



NAVAL POSTGRADUATE SCHOOL

MONTEREY, CALIFORNIA

THESIS

**FRICITION STIR PROCESSING AND FUSION WELDING
IN NICKEL ALUMINUM PROPELLER BRONZE**

by

Michael D. Fuller

March 2006

Thesis Advisor:

Terry R. McNelley

Approved for public release; distribution is unlimited

THIS PAGE INTENTIONALLY LEFT BLANK

REPORT DOCUMENTATION PAGE			<i>Form Approved OMB No. 0704-0188</i>	
Public reporting burden for this collection of information is estimated to average 1 hour per response, including the time for reviewing instruction, searching existing data sources, gathering and maintaining the data needed, and completing and reviewing the collection of information. Send comments regarding this burden estimate or any other aspect of this collection of information, including suggestions for reducing this burden, to Washington headquarters Services, Directorate for Information Operations and Reports, 1215 Jefferson Davis Highway, Suite 1204, Arlington, VA 22202-4302, and to the Office of Management and Budget, Paperwork Reduction Project (0704-0188) Washington DC 20503.				
1. AGENCY USE ONLY (Leave blank)		2. REPORT DATE March 2006	3. REPORT TYPE AND DATES COVERED Master's Thesis	
4. TITLE AND SUBTITLE: Friction Stir Processing and Fusion Welding in Nickel Aluminum Propeller Bronze			5. FUNDING NUMBERS	
6. AUTHOR(S) Michael D. Fuller				
7. PERFORMING ORGANIZATION NAME(S) AND ADDRESS(ES) Naval Postgraduate School Monterey, CA 93943-5000			8. PERFORMING ORGANIZATION REPORT NUMBER	
9. SPONSORING /MONITORING AGENCY NAME(S) AND ADDRESS(ES) N/A			10. SPONSORING/MONITORING AGENCY REPORT NUMBER	
11. SUPPLEMENTARY NOTES The views expressed in this thesis are those of the author and do not reflect the official policy or position of the Department of Defense or the U.S. Government.				
12a. DISTRIBUTION / AVAILABILITY STATEMENT Approved for public release; distribution is unlimited			12b. DISTRIBUTION CODE	
13. ABSTRACT (maximum 200 words) <p>Friction Stir Processing (FSP) is currently being developed for applications including as-cast Nickel-Aluminum Bronze (NAB). Fabrication and repair of the United States Navy's NAB propellers involve fusion welding of as-cast NAB and so it is probable that FSP is likely to encounter as deposited weld metal as well as the more slowly cooled as-cast material. Here, the microstructure and resulting distribution of mechanical properties was examined for a fusion weld overlay, an FSP stir zone and an FSP stir zone that was placed in fusion weld metal. As-deposited weld metal exhibited a refined Widmanstätten morphology and higher yield and ultimate strengths as well as increased ductility in comparison to base metal. However, the heat affected zone (HAZ) exhibited severely reduced ductility. Strength and ductility varied throughout the FSP stir zone. The reduction in ductility in the thermo-mechanically affected zone (TMAZ) and HAZ was less for FSP than for the fusion weld. FSP over a fusion weld resulted in strengths and ductility's similar to those produced by FSP alone, although a region of low ductility was observed at a location where stir zone weld metal and base metal were all present.</p>				
14. SUBJECT TERMS Friction Stir Processing, Fusion Welding NAB Material			15. NUMBER OF PAGES 87	
			16. PRICE CODE	
17. SECURITY CLASSIFICATION OF REPORT Unclassified	18. SECURITY CLASSIFICATION OF THIS PAGE Unclassified	19. SECURITY CLASSIFICATION OF ABSTRACT Unclassified	20. LIMITATION OF ABSTRACT UL	

NSN 7540-01-280-5500

Standard Form 298 (Rev. 2-89)
Prescribed by ANSI Std. Z39-18

THIS PAGE INTENTIONALLY LEFT BLANK

Approved for public release; distribution is unlimited

**FRICTION STIR PROCESS AND FUSION WELDING IN NICKEL ALUMINUM
PROPELLER BRONZE**

Michael D. Fuller
Lieutenant, United States Navy
B.A., University of San Diego, 1992
M.B.A., University of New Haven, 1999

Submitted in partial fulfillment of the
requirements for the degree of

MASTER OF SCIENCE IN MECHANICAL ENGINEERING

from the

**NAVAL POSTGRADUATE SCHOOL
March 2006**

Author: Michael D. Fuller

Approved by: Dr. Terry R. McNelley
Thesis Advisor

Anthony J. Healey
Chairman, Department of Mechanical and Astronautical
Engineering

THIS PAGE INTENTIONALLY LEFT BLANK

ABSTRACT

Friction Stir Processing (FSP) is currently being developed for applications including as-cast Nickel-Aluminum Bronze (NAB). Fabrication and repair of the United States Navy's NAB propellers involve fusion welding of as-cast NAB and so it is probable that FSP is likely to encounter as deposited weld metal as well as the more slowly cooled as-cast material. Here, the microstructure and resulting distribution of mechanical properties was examined for a fusion weld overlay, an FSP stir zone and an FSP stir zone that was placed in fusion weld metal. As-deposited weld metal exhibited a refined Widmanstätten morphology and higher yield and ultimate strengths as well as increased ductility in comparison to base metal. However, the heat affected zone (HAZ) exhibited severely reduced ductility. Strength and ductility varied throughout the FSP stir zone. The reduction in ductility in the thermo-mechanically affected zone (TMAZ) and HAZ was less for FSP than for the fusion weld. FSP over a fusion weld resulted in strengths and ductilities similar to those produced by FSP alone, although a region of low ductility was observed at a location where stir zone weld metal and base metal were all present.

THIS PAGE INTENTIONALLY LEFT BLANK

TABLE OF CONTENTS

I.	INTRODUCTION.....	1
A.	OVERVIEW	1
II.	BACKGROUND	3
A.	NICKEL ALUMINUM BRONZE.....	3
1.	Constitution of NAB	3
2.	Effect of Cooling Rates and NAB Microstructures	3
B.	FRICTION STIR PROCESSING	6
C.	FUSION WELDING.....	8
III.	EXPERIMENTAL PROCEDURES AND TESTING.....	11
A.	MATERIAL.....	11
B.	STATIC ANNEALING	13
C.	MECHANICAL TESTING	14
D.	OPTICAL MICROSCOPY.....	15
E.	SCANNING ELECTRON MICROSCOPY	16
IV.	EXPERIMENTAL RESULTS AND DISCUSSION	17
A.	STATIC ANNEALING	17
B.	FUSION WELD	23
C.	FRICTION STIR PROCESSING	30
D.	FSP 1PASS OVER FUSION WELD.....	37
V.	CONCLUSIONS AND RECOMMENDATIONS.....	51
A.	CONCLUSIONS	51
B.	RECOMMENDATIONS.....	51
	APPENDIX.....	53
	LIST OF REFERENCES	69
	INITIAL DISTRIBUTION LIST	71

THIS PAGE INTENTIONALLY LEFT BLANK

LIST OF FIGURES

Figure 2.1.	Transformation of NAB Phases during Cooling of NAB Material. (From: T. McNelley, NPS)	4
Figure 2.2.	Transformation products of β during equilibrium cooling of NAB. The material shown is NAB in as-cast condition.....	5
Figure 2.3.	Friction Stir Process Illustration	7
Figure 2.4.	Illustrates FSP of NAB process zones. The Stir, Thermo-mechanically Affected Zone (TMAZ) and Heat Affected Zones (HAZ) are delineated.	7
Figure 2.5.	Illustrates the three primary microstructures observed following FSP of NAB. Top left: lamellar; Top right; fine grain; Bottom center. Widmanstätten α	8
Figure 2.6.	Illustrates six pass weld overlay in a machined flat bottom groove with beveled sides on the NAB block provided by NSWC, Carderrock.	9
Figure 3.1.	Image of UNS C95800 NAB Fusion Weld and Friction Stir Processed Block. Test Sample Provided by Naval Surface Warfare Command (NSWC), Carderrock Division.....	12
Figure 3.2.	Schematic of miniature tensile specimen. All dimensions are given in millimeters. Actual thickness of tensile specimens varied based on amount of sample preparation required to remove stress concentrators. All samples were sectioned to have a thickness of 1.4mm.....	13
Figure 3.3.	Illustration of sample sectioning in NAB Block Front View.	14
Figure 4 A.1.1,2.	Figure 4A.1.1 and 2 illustrate the microstructure of as-cast NAB base material when statically annealed at 850°C and 1000°C respectively. Magnification shown is 370X.....	19
Figure 4A.2.	Illustrates the affects of static annealing at various temperatures on ultimate tensile and yield strengths in NAB.	20
Figure 4A.3.	Illustrates the affect of static annealing at various temperatures on ductility.	20
Figure 4A.4.	Illustrates SEM fractography on NAB base material. Both ductile and brittle failure modes are observed.....	21
Figure Set 4A.5.	Illustrates SEM Fractography and ductility data for 850°C statically annealed NAB.	22
Figure Set 4A.6.	Illustrates the SEM Fractography and OM of 1000°C statically annealed NAB material.....	23
Figure 4B.1.	Illustrates the Fusion Weld longitudinal view montage for NAB material.	26
Figure 4B.2.	Illustrates Engineering Stress vs Engineering Plastic Strain data for the center block of fusion welded NAB sample block.	27
Figure 4B.3.	Illustrates 3-dimensional mesh plots for ultimate tensile strength, yield strength and ductility for fusion welded NAB material.....	28

Figure 4B.4.	Illustrates Fusion Weld Fractography and Mechanical Testing Data.	29
Figure 4B.5.	Illustrates Fusion Weld Center Block Optical Microscopy for fracture specimens in Figure 4B.4.....	30
Figure 4C.1.	Illustrates FSP 1Pass optical microscopy, delineating the process zones with a side row of montages taken at 370X.....	33
Figure 4C.2.	Illustrates the Engineering Stress vs Engineering Plastic Strain for the center block of the single pass FSP portion of the NAB sample block.	34
Figure 4C.3.	Illustrates 3-dimensional mesh plots for ultimate tensile strength, yield strength and ductility for single pass FSP NAB material.	35
Figure 4C.4.	Illustrates FSP 1 Pass Fractography and Mechanical Testing Data.....	36
Figure 4C.5.	Illustrates FSP 1Pass Center Block Optical Microscopy for fracture specimens in Figure 4C.4.....	37
Figure 4D.1.	Illustrates a montage of the cross-section view, with respect to FSP direction of the FSP 1 Pass over the Fusion Weld. This montage is taken from the moderate ductility region.....	40
Figure 4D.2.	Illustrates 3-dimensional mesh plots for ultimate tensile strength, yield strength and ductility for FSP 1Pass over Fusion Weld in NAB material.	41
Figure 4D.3.	Illustrates a montage of the cross-section view, with respect to FSP direction of the FSP 1 Pass over the Fusion Weld. This montage is taken from the low ductility region.....	42
Figure 4D.4.	Illustrates the Engineering Stress vs Engineering Plastic Strain for the center block of the single pass FSP over a Fusion Weld portion of the NAB sample block.....	43
Figure 4D.5.	Illustrates FSP 1Pass over Fusion Weld mechanical properties vs depth from the NAB material surface. This data represents the center block only. Additional data is available in Appendix A.....	44
Figure 4D.6.	Illustrates FSP 1 Pass over SEM Fractography and ductility data for the surface specimen (sample #1) sectioned from the center block.....	45
Figure 4D.7.	Illustrates FSP 1 Pass over SEM Fractography and ductility data for the lowest ductility specimen (sample #3) sectioned from the center block.....	46
Figure 4D.8.	Illustrates FSP 1 Pass over SEM Fractography and ductility data for a high ductility specimen (sample #5) sectioned from the center block.....	47
Figure 4D.9.	Illustrates FSP 1 Pass over SEM Fractography and ductility data for a low ductility specimen (sample #6) sectioned from the center block. Note that this samples location corresponds to the HAZ effect seen in other process.	48
Figure 4D.10.	Illustrates FSP 1 Pass over SEM Fractography and ductility data for a moderate ductility specimen (sample #7) sectioned from the center block.....	49

LIST OF TABLES

Table 3.1.	Table gives the chemical composition of UNS C95800 NAB block received from NSWC, Carderrock Division.....	12
Table 3.2.	Polishing Procedure	16

THIS PAGE INTENTIONALLY LEFT BLANK

ACKNOWLEDGMENTS

During the course of this research, extensive amounts of testing and analysis were required to allow a cogent assessment of some of the issues involved with the combination of FSP and fusion welding. I would like to thank Dr. Alex Zhilyaev for his support in helping to get the research started. Also, I extend my special thanks to Dr. Srinivasan Swaminathan for assisting during the later stages of the research and providing invaluable support and guidance. To my thesis advisor, Dr. Terry McNelley, I extend gratitude for his belief in me as a thesis student, patience, support and direction. It was a pleasure working for you, Sir. I hope that the follow-on research in this area has had its foundation strengthened by the work in this document. Lastly, and most importantly, I would like to thank my family, my fiancée Rhonda and my Lord and Savoir Jesus Christ for sticking by me in love and dedication.

THIS PAGE INTENTIONALLY LEFT BLANK

I. INTRODUCTION

A. OVERVIEW

Friction Stir Processing (FSP) is a surface modification technology that can be employed with a myriad of metallic alloys. When applied to cast metals, FSP can eliminate casting defects and improve the mechanical properties of component surfaces. FSP is a derivative of Friction Stir Welding (FSW), a solid state joining process invented by Thomas at TWI in December 1991[1]. FSP, as well as FSW, does not involve exceeding the melting temperature of the metal that is to be processed. FSP utilizes frictional and adiabatic heating to soften the material, while simultaneously exposing it to a stirring action resulting in homogenous mixing and refined grain structures. The metallic surface that results from this process has improved properties, such as increased strength, ductility, and corrosion resistance [2]. FSP is currently being extended to include specific surface engineering applications. The application that is the focus of this research involves the United States Navy's Nickel-Aluminum Bronze as-cast propeller surfaces.

Porosity is inherent in the fabrication of cast components, and it exists throughout the cast material. Fusion weld repair for porosity defects is employed during propeller fabrication processes. However, after the fusion weld is applied, machining of the propeller surface often uncovers additional pores. The result of this is repeated repair cycles that can extend the fabrication period up to 18 months. Once a propeller is placed into service, the erosion of the propeller surface can expose pores and result in inefficiency and increased propeller noise. Again, if fusion welding is utilized, a tedious repair cycle may be involved. Some of the specific issues involved with fusion welding and with FSP will be discussed later. However, fusion welding in fabrication and repair is costly due to the time and labor it involves.

Past research on FSP and fusion weld processes has considered the resulting mechanical properties of each separately. However, with the application of FSP for NAB propeller material, the use of FSP over a previously fusion welded region is highly likely. In addition fusion welds may be used during fabrication and repair for large pores,

subsequently followed by FSP. Given this, it is imperative that the resulting mechanical properties and microstructures be analyzed when combining friction stir processing over fusion welding in NAB cast material. This is the starting point of the research detailed herein.

In the attempt to identify the cost and benefits associated with the combination of FSP and fusion welding, the initial phase of this research consisted of experiments that were designed to allow the deductive separation of thermal effects from mechanical distortion effects on the mechanical properties of NAB material. These experiments involved a series of heat treatments including both air and water quenching, and subsequent tensile testing, optical microscopy and scanning electron microscopy. Of course research in this same vein has been conducted previously. However, the research herein is unique in the sense that the various experiments that were performed were done on the same series of Ni-Al Bronze and all processes performed on this material were done by the same entity- Naval Surface Warfare Center (NSWC), Carderock Division. Furthermore, the distribution of mechanical properties were evaluated by use of miniature tensile test coupons that were obtained by electric discharge machining. These miniature coupons were designed to identify the variations in tensile properties and microstructures throughout the fusion weld zone, stir zones, and the surrounding material. The additional studies that were conducted involved mechanical tensile testing, optical microscopy, and scanning electron microscopy as well. These tests were performed on fusion weld, single-pass friction stir processed, and single-pass friction stir processed over a fusion weld material.

II. BACKGROUND

A. NICKEL ALUMINUM BRONZE

1. Constitution of NAB

Nickel Aluminum Bronze (NAB) is a copper based alloy with aluminum, nickel and iron as the primary alloying additions. The chemical composition of NAB is summarized in Table 3.1. In the development of NAB, Cu-Al alloys were considered due their high strength and ease of casting. However, Cu-Al alloys that contain greater than 9.4wt% Al solidify as a single phase body-centered cubic (bcc) β . When this solidification process involves slow cooling such as that involved in propeller casting, i.e. $\sim 10^{-3}^{\circ}\text{C/s}$, β will transform at a lower temperature in a eutectoid reaction to form face-centered cubic (fcc) α , and an intermetallic gamma (γ) phase. The production of γ results of increased corrosion susceptibility of aluminum-bronze in sea-water environments and reduction in desirable mechanical properties. Because of this, aluminum-bronze propellers are not practical for use in marine environments [3, 4].

By adding nickel and iron at nominally 5% wt. and 4% wt., respectively, the α phase is extended, allowing for an increased amount of aluminum addition without the formation of γ . Also, with the addition of Ni and Fe, intermetallic kappa (κ) phases form from α and β . Some of the benefits from alloying with Ni and Fe at the nominal values stated above are increased strength, wear/abrasion resistance, and fatigue endurance limits [5]. The increase in aluminum content and the formation of κ phases, results in the increase of mechanical properties in NAB materials. It is important to note that above 1000°C , only β is present in NAB.

2. Effect of Cooling Rates and NAB Microstructures

The aforementioned processes occur during equilibrium cooling of NAB at cooling rates of $\sim 10^{-3}^{\circ}\text{C/s}$. However, at high cooling rates, different transformations of β occur. These β transformation products may include martensitic and bainitic constituents, which are typically low in ductility. In addition, α with a Widmanstätten morphology, which is apparently a most desirable constituent for both increased strength and ductility, can result at intermediate cooling rates. In addition, there are four κ phases that may also result during the equilibrium cooling of NAB.

Of the four κ phases that can result during equilibrium cooling of NAB, the κ_i , κ_{ii} , and κ_{iv} phases are iron-rich, having a Fe_3Al composition, and a DO_3 lattice structure. The κ_{iii} phase is nickel-rich and has a lamellar eutectoid form, and NiAl composition, with a B2 lattice structure. (See Fig. 2.2) During analysis of the processed NAB for this research only the κ_i phase was not observed. The κ_i phase is only observed when the NAB's iron content is greater than 5 wt.% [6, 7] (see Table 3.1). The κ_i and κ_{ii} phases are dendritic particles that often have globular shapes. The κ_{ii} phase has been observed to act as a substrate for κ_{iii} formation. The interaction distances in DO_3 κ_{ii} and κ_{iv} , and in B2 κ_{iii} are within about 3%, therefore these phases are difficult to differentiate by diffraction methods alone. Figure 2.1 summarizes the transformations that occur at the equilibrium cooling rate and at higher cooling rates in NAB. The various α phases are indicated and the lamellar $\alpha + \kappa_{iii}$ constituent is also apparent.

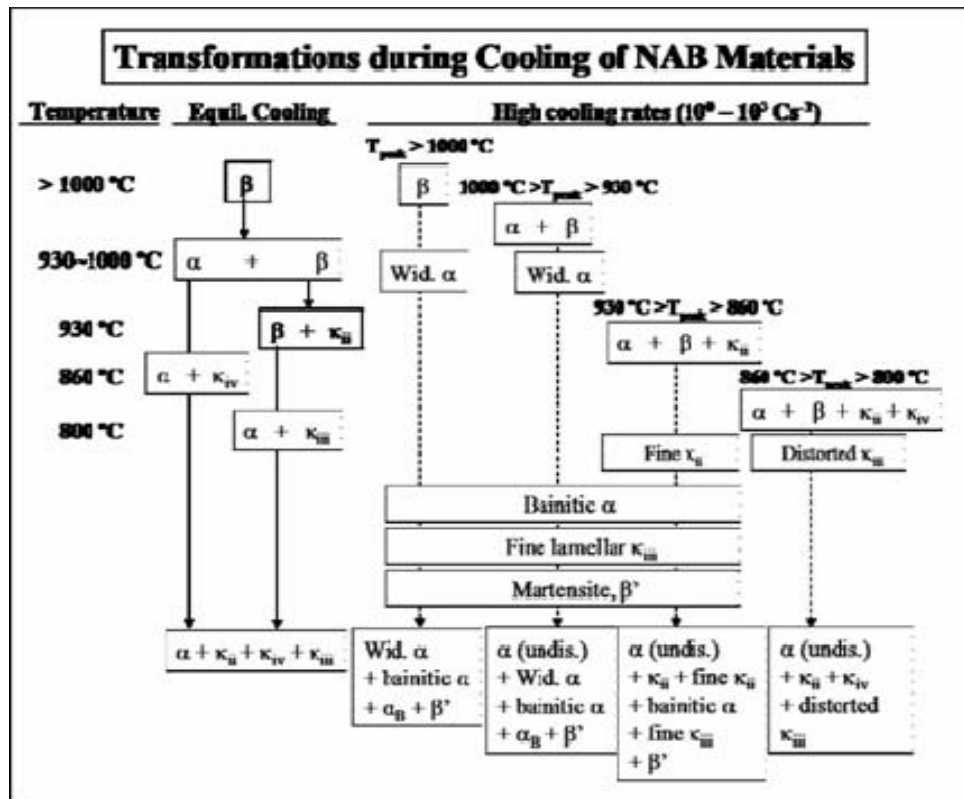


Figure 2.1. Transformation of NAB Phases during Cooling of NAB Material. (From: T. McNelley, NPS)

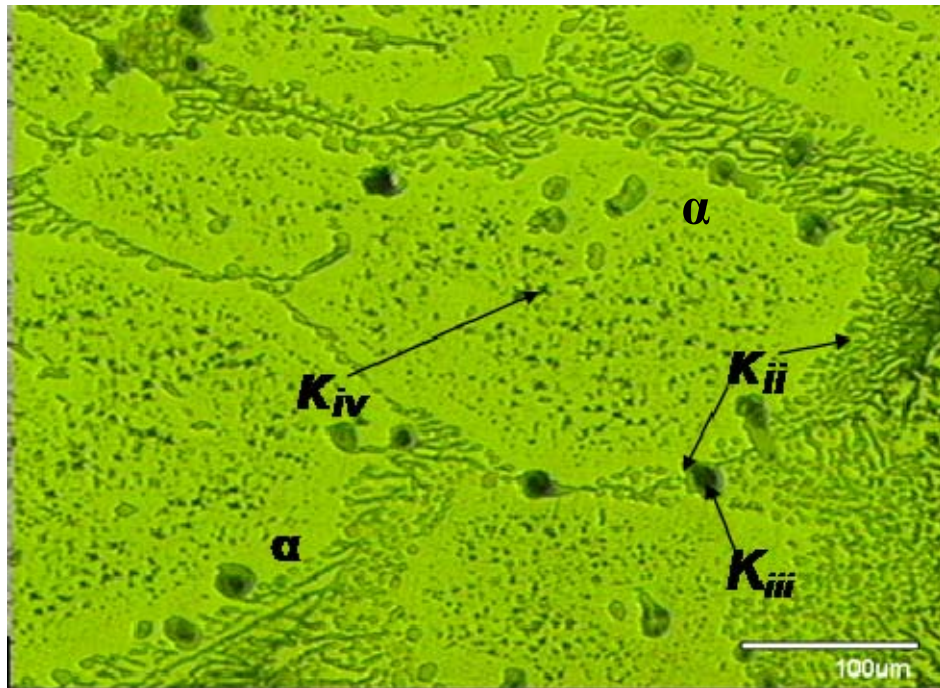


Figure 2.2. Transformation products of β during equilibrium cooling of NAB. The material shown is NAB in as-cast condition.

B. FRICTION STIR PROCESSING

Friction stir processing is a localized, solid state method of modifying the microstructures of near surface layers in a metallic component [8, 9, 10]. This is done via the application frictional and adiabatic heating to soften the material while exposing it to a stirring action. This is accomplished by rotating a tool consisting of a smaller-diameter pin and a larger-diameter shoulder at a prescribed RPM, plunging the tool into the surface of the material until the shoulder is in contact with the surface, then transiting the tool at a certain IPM/velocity through the material (see Figure 2.3). The tool shoulder also acts to constrain the upward flow of material [11]. The result of this action is the production of zones throughout the material (see Figure 2.4). The stir zone is characterized by high strain and strain rates, and refined microstructures. The microstructure refinement and homogenization contribute to increased corrosion resistance and even super-plasticity in some materials [11]. The thermo-mechanically affected zone (TMAZ), is located just outside the stir zone (SZ), and is characterized by the appearance of distorted base metal grains due to relatively small deformation and lesser heating. The darker etched areas in this region are β transformation products formed as a result of the reversion of $\alpha + \kappa_{iii}$ as temperatures rise above 800°C followed by rapid cooling after the transiting of the tool [11]. The heat affected zone (HAZ) is the interface between the processed zones and as-cast based material, and is generally characterized by low ductility. The temperatures that are reached in the stir zone are important in determining the extent and type of β transformation products that will result. It has been noted that in some NAB alloys when temperature is above 1000°C, only β is present. Subsequently, upon cooling, the type of β transformation products will depend on the cooling rate that is experienced. Equilibrium cooling (10^{-3} °C/s) will give κ_{iv} , κ_{ii} , and κ_{iii} , while accelerated cooling yields the aforementioned in addition to Widmanstätten α morphology, or Bainitic α , or even Martensitic β' . Figure 2.5 illustrates the three fundamental microstructures associated with the friction stir processing of NAB.

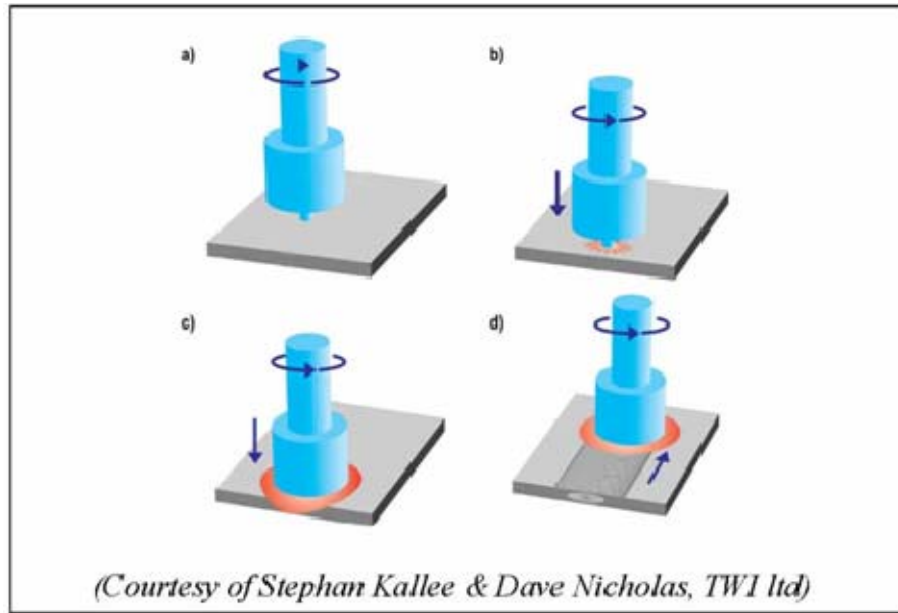


Figure 2.3. Friction Stir Process Illustration

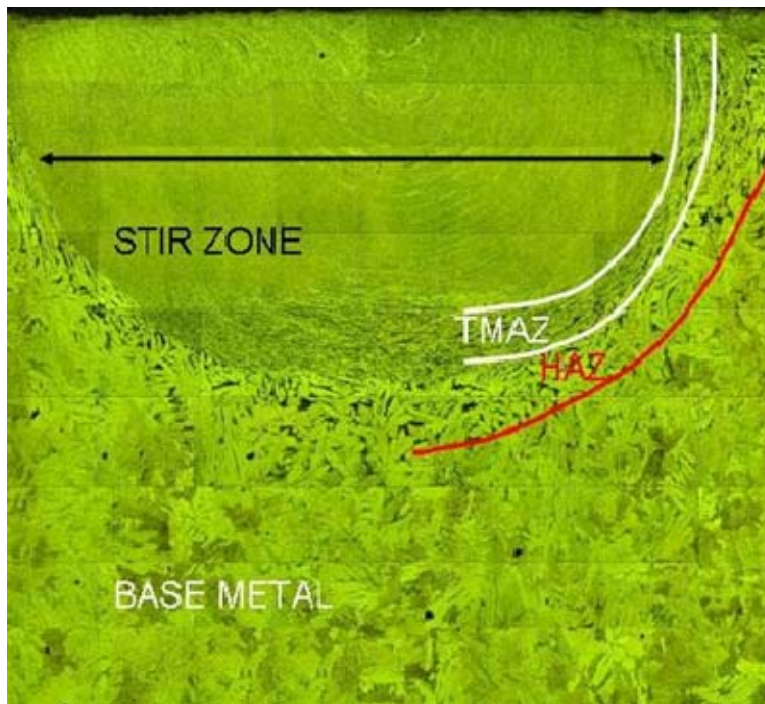


Figure 2.4. Illustrates FSP of NAB process zones. The Stir, Thermo-mechanically Affected Zone (TMAZ) and Heat Affected Zones (HAZ) are delineated.

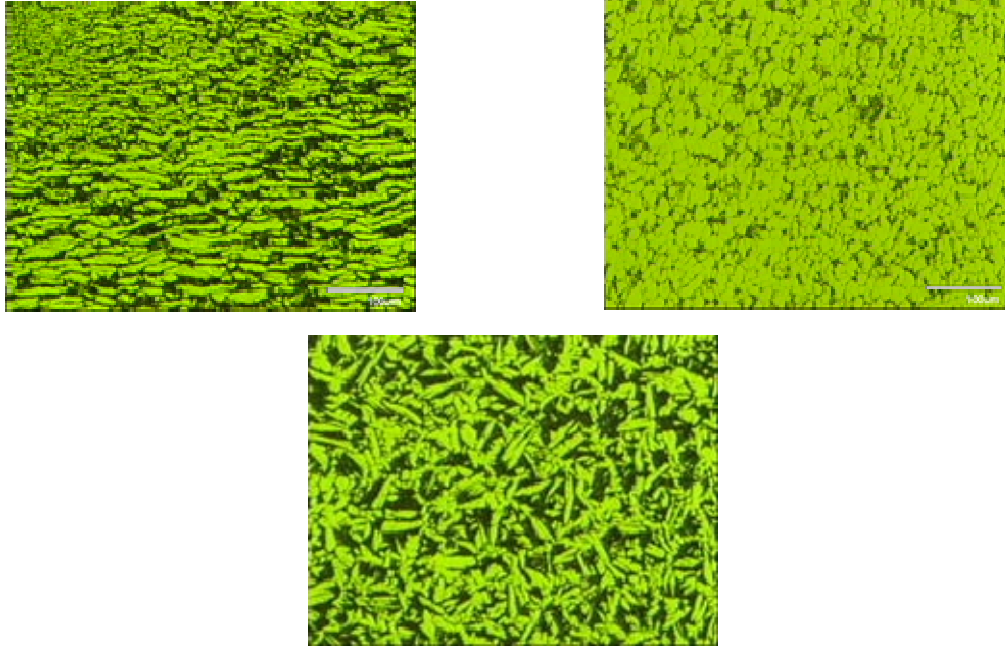


Figure 2.5. Illustrates the three primary microstructures observed following FSP of NAB. Top left: lamellar; Top right; fine grain; Bottom center. Widmanstätten α

C. FUSION WELDING

Gas-metal arc welding (GMAW) was used to provide the weld overlays on the NAB plate provided by NSWC Carderrock. GMAW is widely used in welding of metallic materials that require only inert gas protection of weld metal (i.e., many aluminum alloys) [12]. The GMAW overlay was primarily intended to simulate the fusion weld repair of a NAB surface and not joining of NAB material. Nevertheless, the issues that are inherent in raising the temperature of the metal above its melting temperature (T_{melt}), followed by subsequent cooling and re-solidification are still present. The most prevalent of these are the effects of constitutional supercooling in alloys and solidification cracking. In essence, constitutional supercooling in alloys results in departure of the solid/liquid (S/L) interface from a planar morphology to cellular, columnar dendritic, or equiaxed dendritic [8,9]. Departing from planar morphology to cellular or dendritic, results in segregation of solutes and reduced weld ductility. Solidification cracking, occurs during the later stages of solidification [10]. Cracks are introduced by stresses that result from thermal gradients and insufficient liquid in the

weld zone. These tensile stresses are directional and are inevitably applied across grain boundaries. When these stresses exceed the strength of the nearly solidified weld metal, cracking is induced.

Solidification cracking is also observed in casting as well as in fusion welding [10]. Critical to the severity of both aforementioned issues is cooling rate. In the NAB sample plate, there was no pre-heating. However, six weld passes were performed. The plate was not allowed to cool to ambient between successive passes and so cooling rates were lower on the later passes. In other words, with each successive pass, the amount of heat input into the material was increased, resulting in a raised T_o , and a lower cooling rate (see equation 3.1). For the weld pass configuration, see Figure 2.6.

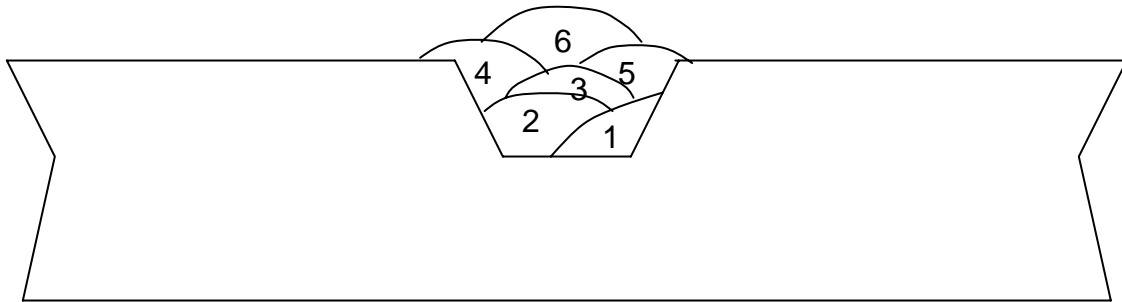


Figure 2.6. Illustrates six pass weld overlay in a machined flat bottom groove with beveled sides on the NAB block provided by NSW, Carderrock.

THIS PAGE INTENTIONALLY LEFT BLANK

III. EXPERIMENTAL PROCEDURES AND TESTING

A. MATERIAL

A UNS C95800 NAB as-cast plate was provided by NSWC Carderrock Division, Bethesda, Maryland. The plate has the following dimensions: width- 14.85cm; thickness-3.46cm; length-~32.9cm.(Fig.3.1) Three stages were involved in processing the plate. Initially, a groove was machine in the plate along its longitudinal axis down the centerline. The groove dimensions are: width-1.6cm; depth .6cm-; length-32.9cm. Following the machining, a Miller Delta Weld 651 CV machine was used to place a six pass Gas Metal Arc Weld (GMAW) in the groove. The weld passes were ~33cm in length. The electrode was Amptrode 46, which has a similar composition as the NAB plate. The welding was conducted at 24.5V and 239Amps. The travel speed during welding was 8.5 IPM. The chemical composition of the NAB plate is detailed in Table 3.1. No preheating was used prior to commencing the welding process, and so the cooling rate of the weld and surrounding material was a maximum after the first pass. The average weld time per pass (six passes total) was ~90sec, so the initial temperature increased during welding. From Rosenthal's 3-dimensional equation the cooling rate along the weld center line behind the heat source is given by [12]:

$$\frac{\partial T}{\partial t} = -2\pi kV \frac{(T - T_0)^2}{Q} \quad (3.1)$$

where: k= thermal conductivity

V= weld speed

T= temperature

T₀= starting temperature of material to be welded (will change with each successive pass). From equation 3.1 the cooling rate decreases as T₀ increases.

Once the welding was complete along the entire longitudinal axis of the plate, the sections that were to contain single pass and multi-pass friction stir processing were machined to attain a flat surface. This flat surface was then exposed to a single pass and 4-step raster multi-pass friction stir process, using a ¼ inch step spiral pin that was

transited across the NAB block at 3 IPM and rotating at 1000 RPM. Figure 3.1 illustrates the aforementioned processes.

Element	Base Chemistry	MIL STD: MIL-B-24480A
Copper	81.8	79 min
Aluminum	8.72	8.5-9.5
Nickel	4.31	4.0-5.0
Iron	3.59	3.5-4.5
Silicon	0.42	0.10 max
Manganese	1.41	0.8-1.5
Tin	0.017	-----
Carbon	0.007	-----
Sulfur	0.003	-----
Phosphorus	0.011	-----
Lead	0.0029	0.03 max
Tungsten	<0.002	-----

Table 3.1. Table gives the chemical composition of UNS C95800 NAB block received from NSWC, Carderrock Division

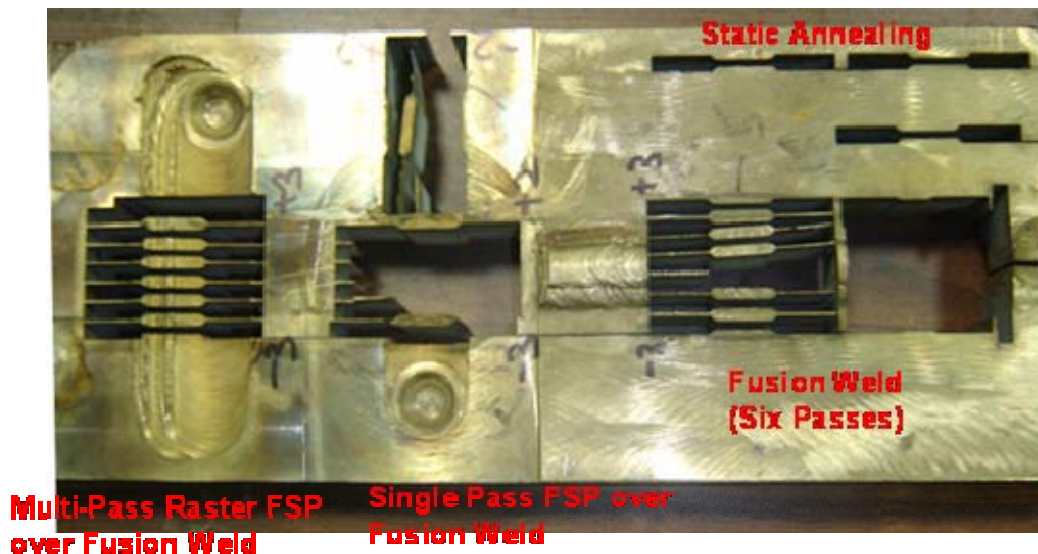


Figure 3.1. Image of UNS C95800 NAB Fusion Weld and Friction Stir Processed Block. Test Sample Provided by Naval Surface Warfare Command (NSWC), Carderrock Division.

As indicated in the illustration, tensile blocks were sectioned from the various processed areas with the intent of conducting detailed analysis of the microstructure and mechanical property relationship associated with the various processes. Particular attention was to be given to variation of tensile properties with location in the various process zones. An illustration of the tensile specimens that were sectioned can be viewed in Figure 3.2.

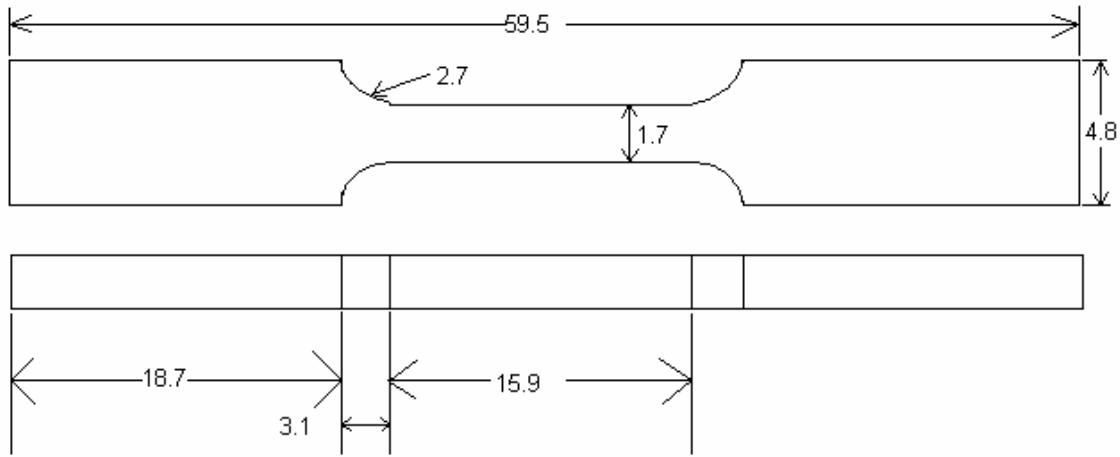


Figure 3.2. Schematic of miniature tensile specimen. All dimensions are given in millimeters. Actual thickness of tensile specimens varied based on amount of sample preparation required to remove stress concentrators. All samples were sectioned to have a thickness of 1.4mm.

B. STATIC ANNEALING

Static annealing was conducted on selected tensile specimens. The annealing temperatures ranged from 800°C to 1000°C. The annealing was conducted using a Linberg Furnace Model 51442, which has ratings of 4880W and 240V, with maximum temperature capability of 1200°C. The furnace was brought up to the annealing temperature and stabilized. Temperature monitoring inside the furnace was accomplished by using a mounted temperature monitoring device. Subsequently, the sample was placed into the furnace on a heat resistant ceramic bed, and a Digi-Sense Model 8528-40 thermocouple was used to monitor the sample's temperature. The samples temperatures were measured by placing the thermocouple wire through a breach in the furnace cover. The breach was designed for this purpose. Once the thermocouple reading stabilized for the tensile specimen, a 30 minute hold was commenced. At the

completion of the 30 minute hold at annealing temperature, the sample was removed from the furnace, and either air cooled or immersed in a container of room-temperature water for quenching.

C. MECHANICAL TESTING

Mechanical testing consisted of over 300 tensile tests of miniature tensile samples (see Figure 3.2). These miniature tensile samples were sectioned using a Charmilles Andrew EF630 electric discharge machine (EDM). The EDM was used to extract tensile specimen blanks. Subsequently, these blanks were sliced to provide miniature samples that were sectioned vertically from the surface to the bottom of the NAB plate to allow identification of the distribution microstructure and mechanical properties throughout the material (see Figure 3.3). The EDM wire used has a diameter of 0.30mm. Therefore, ~0.30mm of material is estimated as lost during each cutting evolution.

FRONT VIEW OF SAMPLE SECTIONING

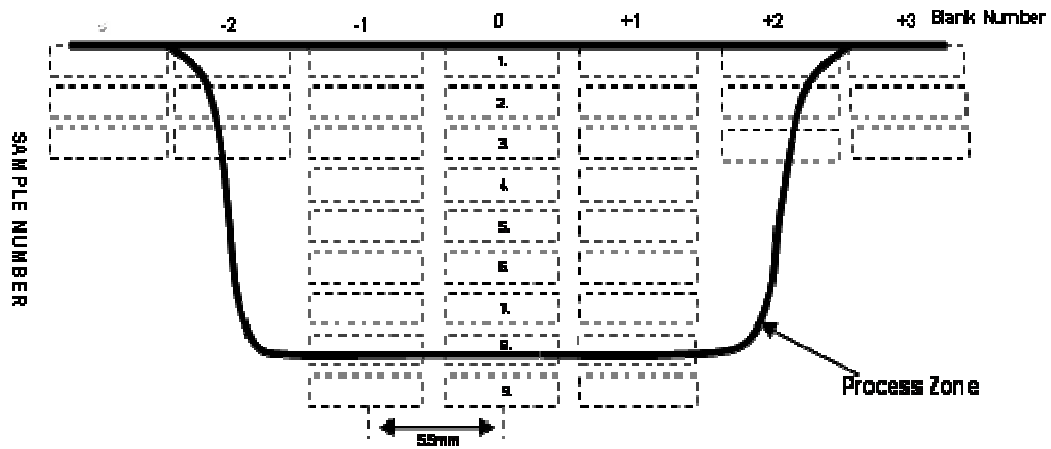


Figure 3.3. Illustration of sample sectioning in NAB Block Front View.

The sectioned miniature tensile specimens were prepared for tensile testing by carefully removing stress concentrators and surface residue due to EDM cutting, by light sanding with 400 grit SiC paper. Tensile testing was conducted with an INSTRON Model 4507 machine with GPIB interface control. The INSTRON Series IX software was used to control the machine and collect and process the data. Upon loading, the tensile specimens were carefully centered and secured by tightening one portable grip connected to a universal joint, around the one end of the specimen's grip section. The

portable grip containing the tensile specimen was meticulously aligned in the INSTRON machine, and the other tensile grip was secured in a fixed miniature vice, so that the tensile specimen was configured in the vertical position. From this point, the samples were loaded to failure by constant displacement of the lower fixed grip in the downward direction. Following the pull of each sample the cross-arm providing the constant downward displacement was zeroed, the load cell and extension length were reset and balancing at the INSTRON control panel was conducted. The text files that were created by the software data collection resulted in force/displacement matrices that were later input into a Matlab Version 6.5 program design to convert this raw data into engineering stress vs engineering plastic strain curves. Within the Matlab program allowance was made for the elasticity of the INSTRON machine parts and the grips used. This was necessary because of the inability to use an extensometer during miniature sample testing.

D. OPTICAL MICROSCOPY

Optical Microscopy (OM) was used to evaluate the grain structure and morphologies of selected cross sections and tensile samples. Cross-sectional and/or longitudinal montages were created for the fusion weld, single pass friction stir processed material, and fusion weld material subjected to single pass friction stir processing. A Carl Zeiss JENAPHOT 2000 was used to perform optical microscopy. The microscope provided visual output via a PULNIX TMC-74-CCD camera. Also, a digital output was provided to allow for capture of digital images and the formulation of montages. The software that was used for this purpose is SEMICAPS photo capturing and measurement software.

The preparation of the cross-sections and tensile samples for OM involved sectioning the samples using the EDM, followed by mounting them in red phenolic discs. These mounted samples were polished using Table 3.2. The polishing was accomplished using ECOMET 3 and ECOMET 4 polishing wheels along with the AUTOMET 2 powerhead. Subsequent to steps 4-7, the mounted samples were ultrasonically cleaned in methanol for 15 minutes and then blown dry prior to proceeding to the next polishing step. On several occasions steps 4-7 would have to be repeated to remove surface scratches that were visible during optical microscopy. The etching of the sample

occurred in two steps, utilizing two separate etching solutions. Etching solution #1 contains 40ml ammonium hydroxide, 40ml of water, and 2ml of hydrogen peroxide. The sample was etched in the first etching solution for 2-3 seconds, rinsed with water, and then etched in the second etching solution. Etching solution #2 contains 30ml of phosphoric acid, 60ml of water, and 10ml hydrogen peroxide. Several montages were produced as a result of the optical microscopy performed.

Step	Abrasive	Time	RPM
1	400 Grit SiC Paper	5 min.	90
2	1000 Grit SiC Paper	5 min.	90
3	2400 Grit SiC Paper	5 min.	90
4	4000 Grit SiC Paper	5 min.	90
5	3 Micron Metadi Diamond Suspension	15 min.	150
6	1 Micron Metadi Diamond Suspension	15 min.	150
7	0.05 Micron Colloidal Silica	15 min.	40

Table 3.2. Polishing Procedure

E. SCANNING ELECTRON MICROSCOPY

Scanning electron microscopy (SEM) was conducted using a Tobcon Model SM-500/510 (SEM), operating in the secondary electron imaging mode to identify the prevalent fracture mode for failed tensile specimens. The tensile specimens were chosen with particular attention to those that displayed low ductility. The samples just above and below the low ductility sample were also analyzed. This was done for selected fusion weld, single pass friction stir process, fusion weld subjected to a friction stir process, and annealed base material.

IV. EXPERIMENTAL RESULTS AND DISCUSSION

A. STATIC ANNEALING

The annealing studies were conducted over a series of temperatures ranging from 800°C to 1000°C. The cooling rate of the air-cooled samples was $\sim 3^{\circ}\text{C/s}$, from the observation that the samples required approximately 5 minutes to cool to ambient temperature. This rate exceeds that for equilibrium cooling for NAB. As a result, the ‘high cooling rate’ β transformation products (i.e., Widmanstätten α , Bainitic α , or even Martensitic β') will be observed and the dark-etched areas of the optical micrographs in Figures 4A.1.1 and 2 will be designated as ‘ β transformation products’ only.

Figure 4A.1.1 shows that as temperature increases above 800°C, the lamellar $\alpha+\kappa_{\text{iii}}$ reverts to solution. Nickel and aluminum from the $\alpha+\kappa_{\text{iii}}$, diffuse into the surrounding material and result in the formation of β . Subsequently, the cooling rate that is experienced after the 30 minutes annealing, results in the formation of β transformation products, as illustrated by the dark etched areas. The dark particles in Figure 4A.1.1 may be un-dissolved κ_{ii} . The dark-etching regions in this micrograph suggest that time-at-temperature was insufficient for homogenization of nickel and aluminum in the β formed during heating.

Figure 4A.1.22 illustrates the transformation products of β (dark etched areas), and primary α (light areas), without the presence of κ particles due to their complete dissolution. According to past studies, at temperatures of 1000°C or more, the complete transformation to β should occur[11]. The more uniform appearance of β is a function of both the aforementioned temperature range and the time period for which this temperature range is held. The fact that the complete transformation to β is not observed is a function of alloy composition.

After the annealing of various tensile samples was conducted, mechanical tensile test were performed and the resulting mechanical properties for base material and for each annealing temperature were recorded and plotted. A summary of this data can be found in Appendix A. Two sets of data that will be reviewed are for 850°C and 1000°C.

Figure 4A.3 and 4 illustrate the affects on static annealing on the mechanical properties of NAB. Ultimate tensile strength for NAB material increases with annealing temperature, while ductility is lowest for the highest annealing temperature-1000°C, and highest for 850°C. The ductility for the 1000°C sample suggests that the β transformation products illustrated by the dark etched areas of Figure 4A.1.2 are Bainitic α , or even Martensitic β' . The high ductility at 850°C may reflect lower fraction of β transformation products. This is consistent with the flow diagram illustrated in Figure 1.1. In addition, the increased ductility at 850°C may also be attributed to recovery of residual stress effects introduced during casting of the material.

Figure 4A.3 illustrates that ultimate tensile strength (UTS) increases over all annealing temperatures, while yield strength for annealed conditions is less than base material until ~ 850°C.

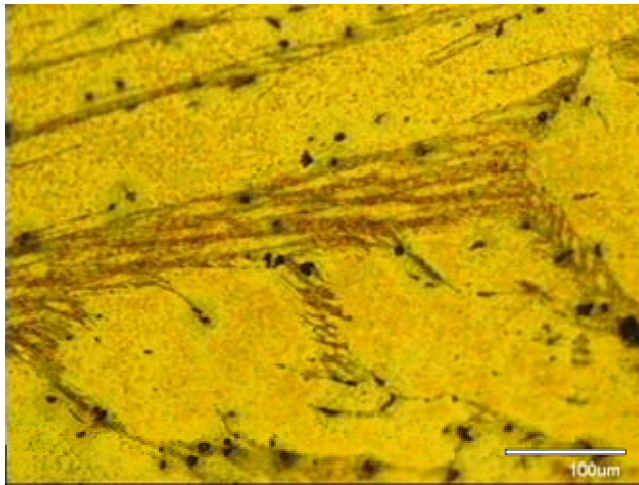
Figure 4A.4 illustrates the ductility of annealed NAB is above the base material ductility until ~870°C, at which temperature it decreases until it reaches its minimum value ~4.5% following annealing at 1000°C. Altogether, these results suggest that increased fractions of β transformation products involving Bainitic α , and even Martensitic β' constituents are detrimental to ductility.

Figure 4A.5 illustrates the SEM fractography for the base material. In this figure it is apparent that both brittle (cleavage) and ductile failure (microvoid formation and coalescence) modes are present on the tensile specimen fracture surface. The average ductility measured for the base material was ~9.5%.

Figure 4A.6 illustrates the SEM fractography and ductility data for the material statically annealed at 850 °C. The microvoids are both elongated and equiaxed, and the fraction of cleavage cracking appears to have decreased compared, to that observed in the base metal fracture surface. This would indicate that the mode of failure experienced for the 850°C annealed tensile specimen was more ductile in nature than the base sample. The mechanical data supports this in that the average ductility for 850°C annealed tensile samples is 11.13%.

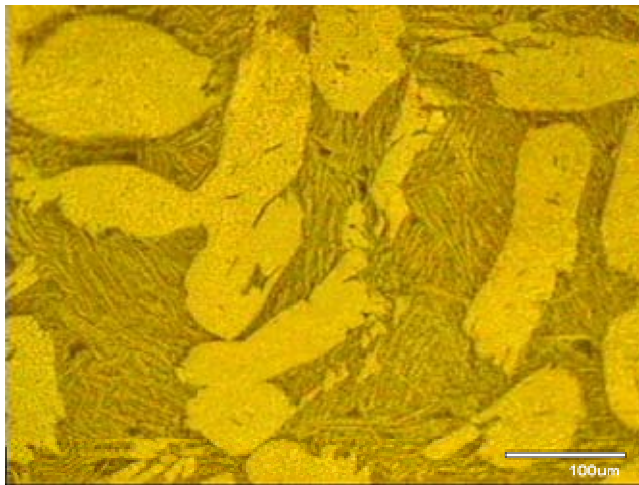
Figure 4A.7 illustrates the SEM fractography, optical microscopy and ductility for NAB material statically annealed at 1000°C. The SEM fractography shows large

fractions of cleavage and few areas of ductile fracture. A primary α band and Prior β band are delineated. These two bands have a shared interface that appears to be a crack. In addition, cracks are apparent in the OM taken on the same tensile specimen. As discussed earlier, β transformation products have not been conclusively identified, but are likely to be Bainitic or Martensitic in nature.



850°C

4A.1.1



1000°C

4A.1.2

Figure 4 A.1.1,2. Figure 4A.1.1 and 2 illustrate the microstructure of as-cast NAB base material when statically annealed at 850°C and 1000°C respectively. Magnification shown is 370X.

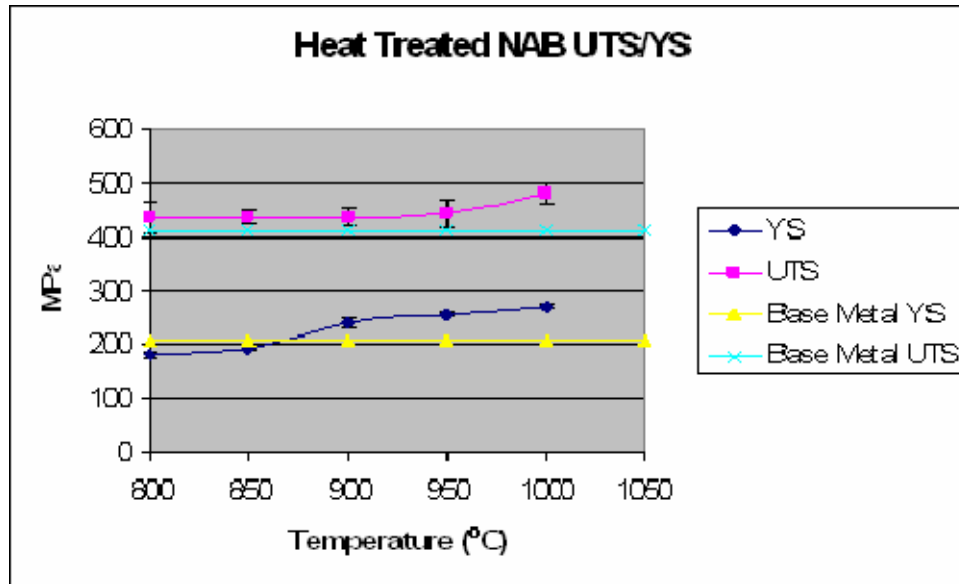


Figure 4A.2. Illustrates the affects of static annealing at various temperatures on ultimate tensile and yield strengths in NAB.

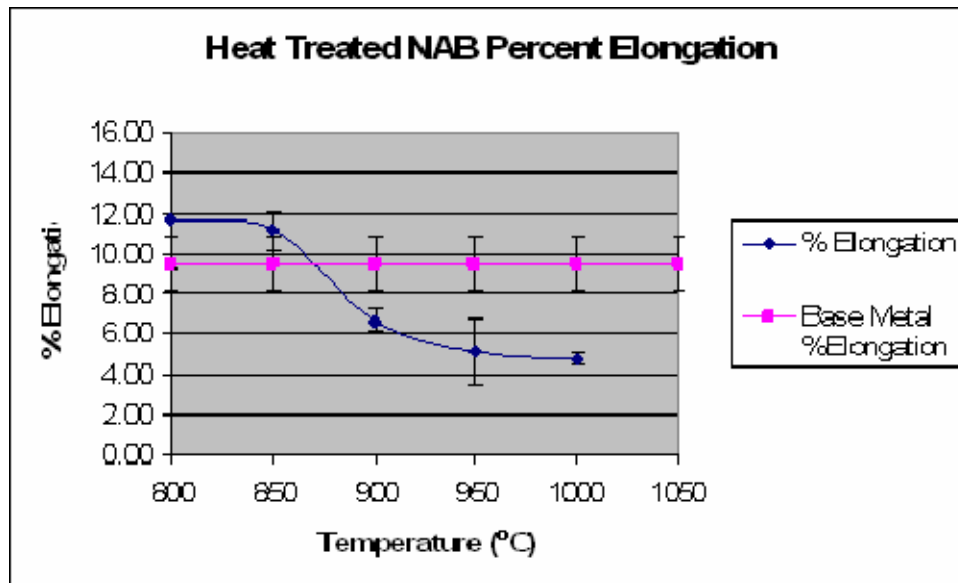


Figure 4A.3. Illustrates the affect of static annealing at various temperatures on ductility.

NAB Base Material

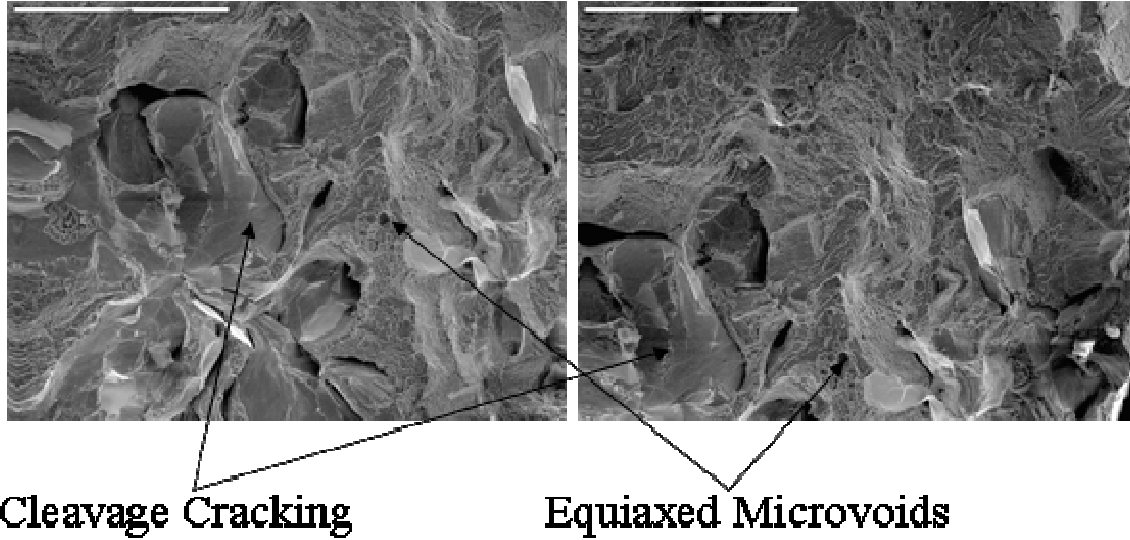


Figure 4A.4. Illustrates SEM fractography on NAB base material. Both ductile and brittle failure modes are observed.

850°C Statically Annealed NAB

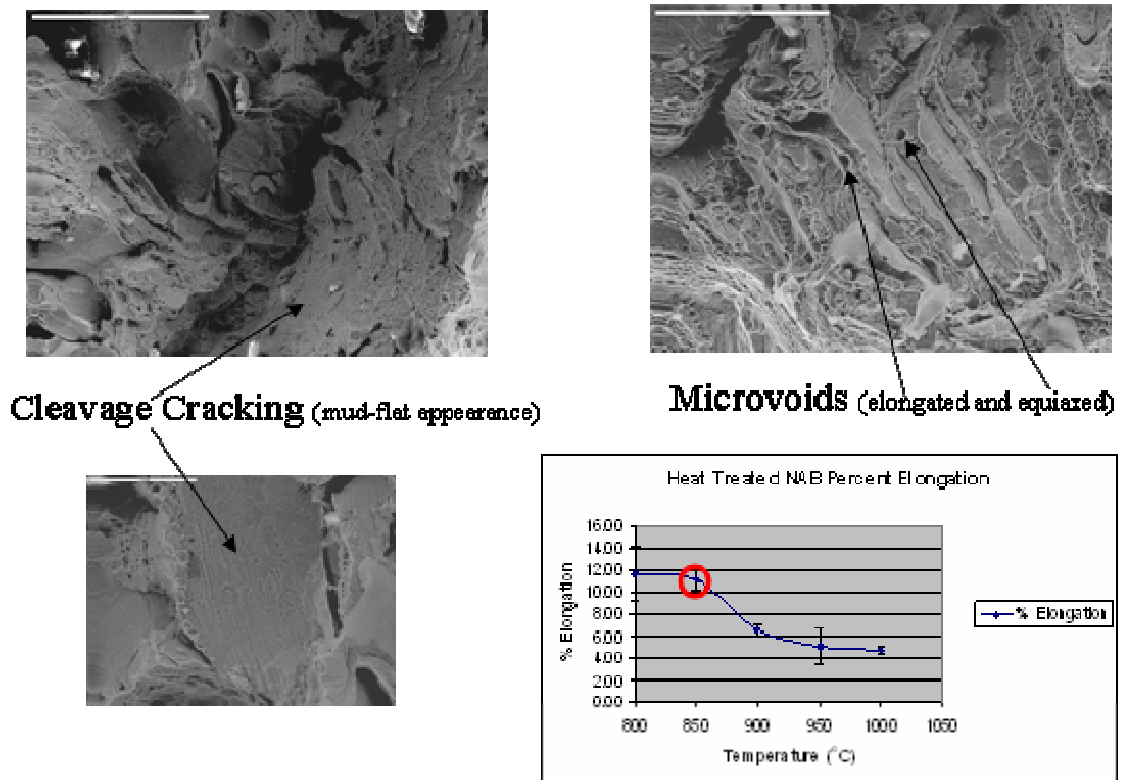


Figure Set 4A.5. Illustrates SEM Fractography and ductility data for 850°C statically annealed NAB.

1000°C Statically Annealed NAB

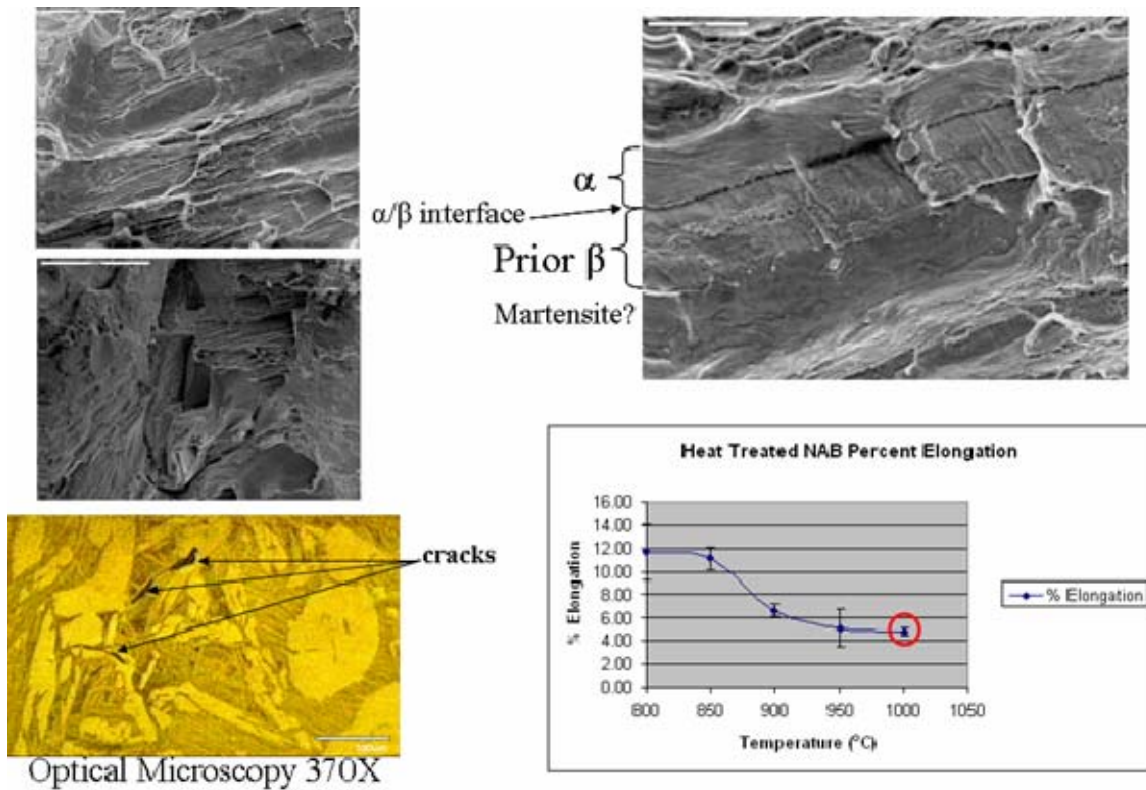


Figure Set 4A.6. Illustrates the SEM Fractography and OM of 1000°C statically annealed NAB material.

B. FUSION WELD

Six GMAW passes were performed (see Figure 2.4) on the as-cast NAB plate. The tensile samples that were sectioned from the fusion weld portion of the plate were aligned parallel to the weld's axis of travel. The data that is presented and analyzed in this section is for the fusion weld with particular emphasis on the center block. Seven blocks of data that were collected, and they are illustrated in the Appendix.

Figure 4B.1 illustrates a montage of images of the longitudinal section from the weld. Four areas of varying morphology are shown here. Melting temperature for this NAB alloy is ~1070°C. Upon cooling the liquid re-solidified at this temperature. Just below this temperature, the alloy is expected to be entirely β . Rapid cooling will occur in welding. The cooling rate will decrease with each successive pass. Slower rates will form the transformation of β to Widmanstätten α . Transiting down the montage, starting

at the top of the fusion zone, Widmanstätten α is present but becomes finer with depth. This likely reflects that the heat input that with each successive pass, allows for the coarsening of Widmanstätten α . Region two of the montage reveals the fusion line. Outside the fusion line is the HAZ. The HAZ microstructure is characterized by large primary α grains that contain κ_{iii} and κ_{ii} particles. The primary α grains are surrounded by dark etched areas which represent β transformation products. The β transformation products are most likely bainitic α or martensitic β' in nature. Region four is base NAB material.

Figure 4B.2 illustrates engineering stress vs. engineering plastic strain for the fusion welded material. The ductility of the fusion weld material is high when compared to the base material. Indeed, the solidified weld metal is also higher in yield and ultimate strengths and, so, this filler material over-matches the base metal properties. Deeper into the material in regions two and three at the fusion line, the ductility decreases drastically. From annealing study, at 1000°C reduced ductility was also observed. Upon further observation of the optical and scanning electron microscopy results, the morphology and fracture surface data show that bainitic and martensitic products are evident. The cooling rate in the HAZ is likely similar to that experienced in the annealing studies due to amount of surrounding cold metal that is contained in the NAB sample block.

Figure 4B.3 summarized in a three dimensional representation, the mechanical data acquired over the entire fusion weld area. As stated earlier, seven blocks of data were acquired and they are all represented here in these mesh plots. Of particular interest here is that both ultimate and yield strengths are higher than the base material. It is evident that yield strength is somewhat less uniform throughout the breadth of the material, and slightly lower for this process when compared to FSP. The ductility in the fusion zone is highest along the center-line and tapers off at the outer edges of fusion zone.

Figure 4B.4 illustrates fusion weld SEM fractography and mechanical testing data for the center of the fusion weld. The SEM fractography displays the fracture surfaces for the lowest ductility sample in the region (sample 7) and the neighboring samples (6 and

8). Also displayed in the corner of the SEM fractography are profiles of the fractured tensile specimen via optical microscopy. The fracture surface profiles for samples 6 and 8, are indicative of ductile fractures, while the profile for sample 7 is irregular and represents brittle fracture. The ductility plot supports the optical microscopy profile views and SEM fractography. Sample 6 and 8 fracture surfaces display a higher fraction of microvoid formation and coalescence, while sample 7 which is located just outside the fusion line, has a surface that contains a notably higher fraction of cleavage cracking in some locations, and a mud-flat appearance.

Figure 4B.5 illustrates fusion weld microstructures at higher magnification, from locations near the fracture specimen's side profiles. The grain structure reveals for sample 6 is a morphology that is primarily Widmanstätten α , explaining the higher strength and ductility properties. Sample 7, the lowest ductility sample, contains a grain structure that has elongated or distorted α grains, with the presence of κ_{iv} , κ_{ii} , and κ_{iii} particles and a relatively large fraction of dark etched β transformation products. Sample 8 displays elongated or distorted α grains, similar to those present in sample 7. However, a larger fraction of κ_{iv} , κ_{ii} , and κ_{iii} particles have come out of solution. In essence, sample 7 and 8 are representative of that region that contains and borders the solid/liquid interface. It is apparent that the material at the interface had to reach T_{melt} and consequently, upon re-solidification can be compared to the effects of the static annealing study at 1000°C. This can be done given that the cooling rates for the static annealing and the solid/liquid interface are roughly similar. Given this, it may be deduced that the thermal cycle in this region, namely peak temperature and cooling rate, contribute to the resulting mechanical properties through formation of low ductility transformation products of β .

Fusion Weld Montage (Longitudinal View)

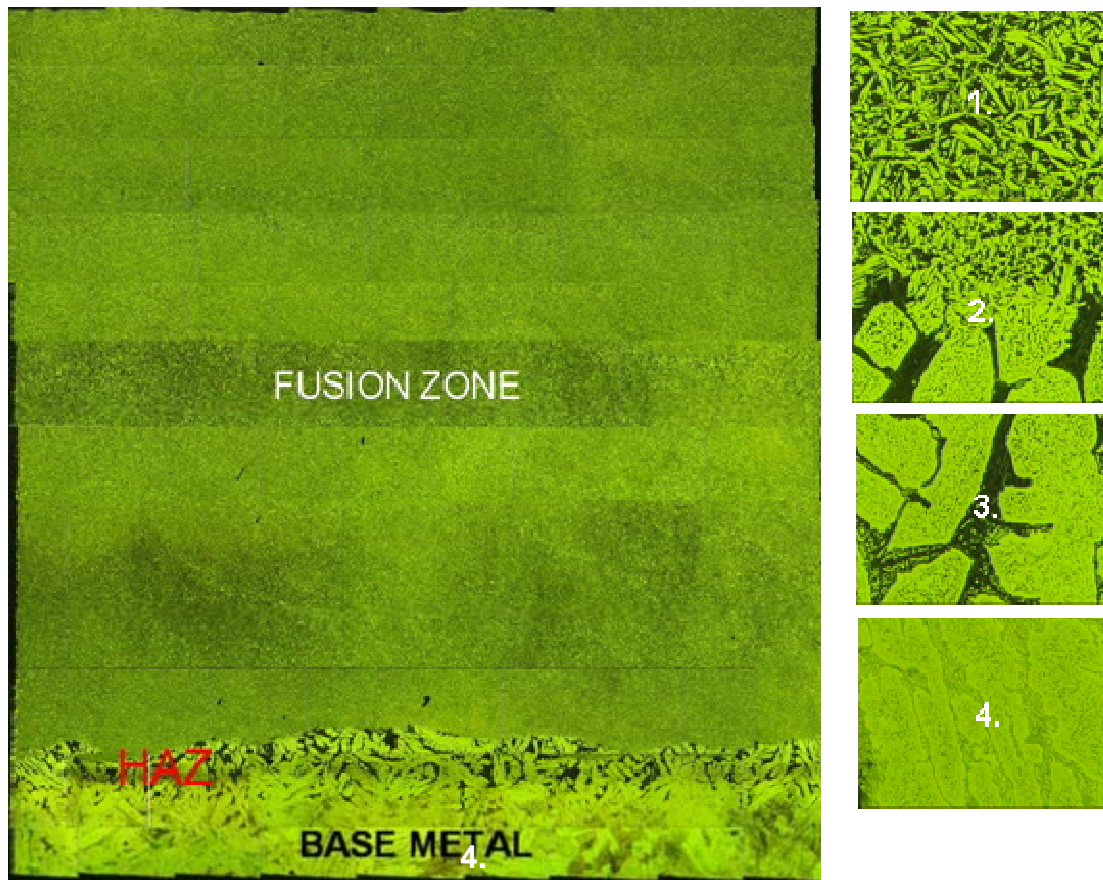


Figure 4B.1. Illustrates the Fusion Weld longitudinal view montage for NAB material.

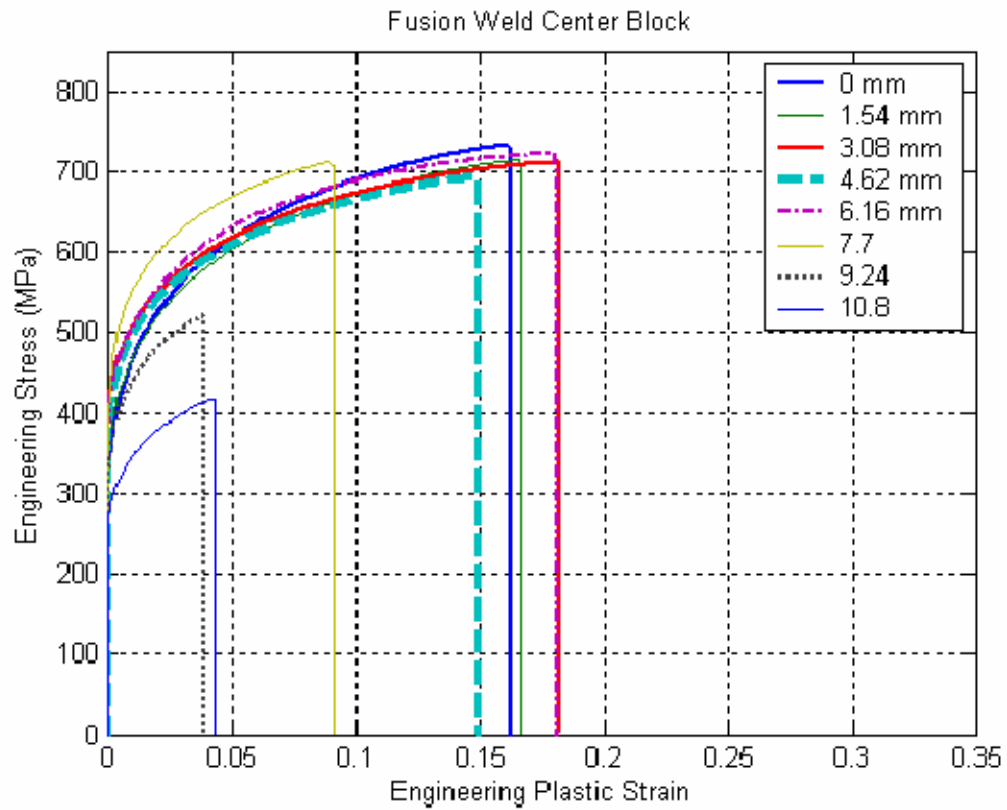


Figure 4B.2. Illustrates Engineering Stress vs Engineering Plastic Strain data for the center block of fusion welded NAB sample block.

FW

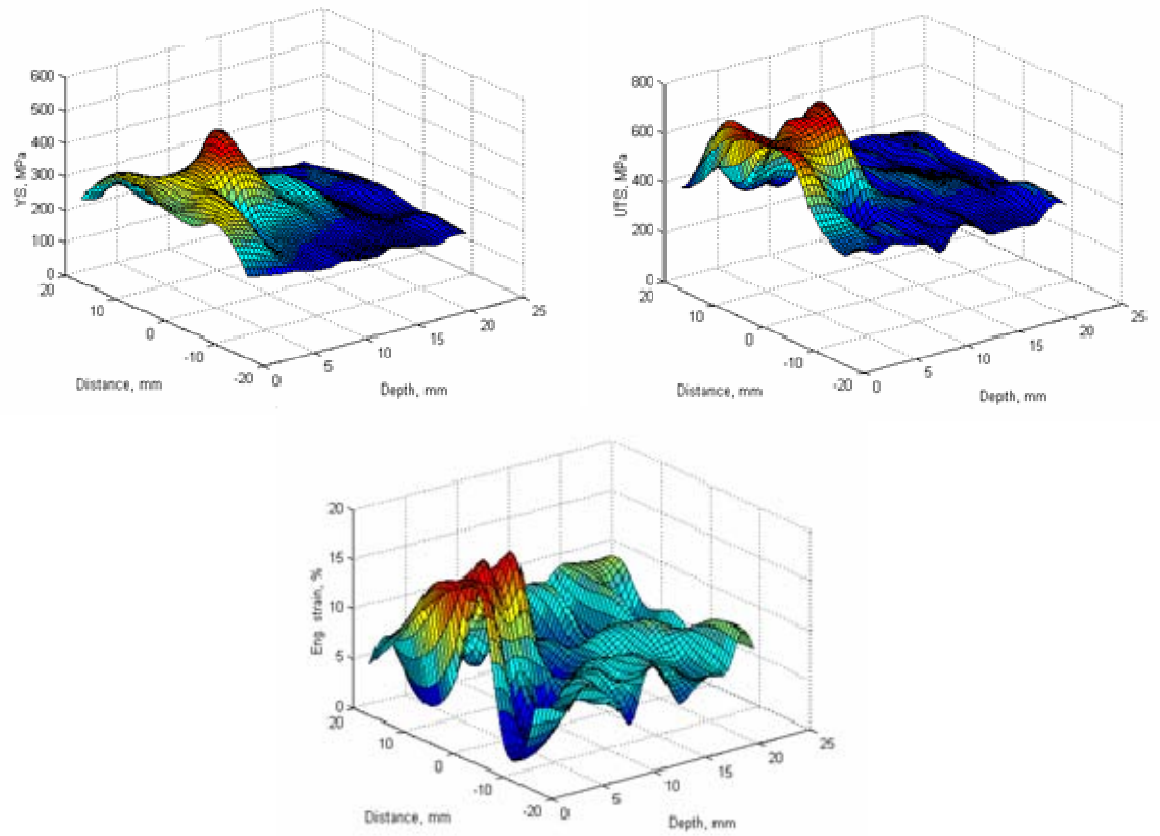


Figure 4B.3. Illustrates 3-dimensional mesh plots for ultimate tensile strength, yield strength and ductility for fusion welded NAB material.

Fusion Weld SEM Fractography/ Mechanical Data

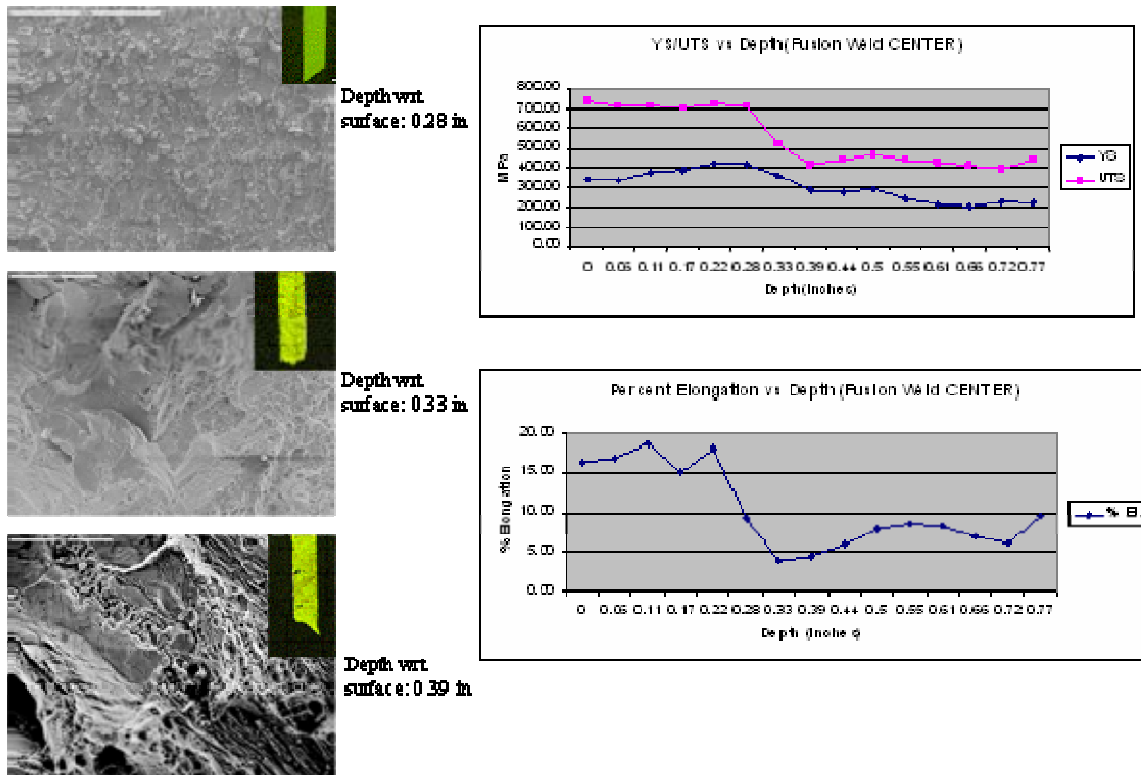


Figure 4B.4. Illustrates Fusion Weld Fractography and Mechanical Testing Data.

Fusion Weld Optical Microscopy

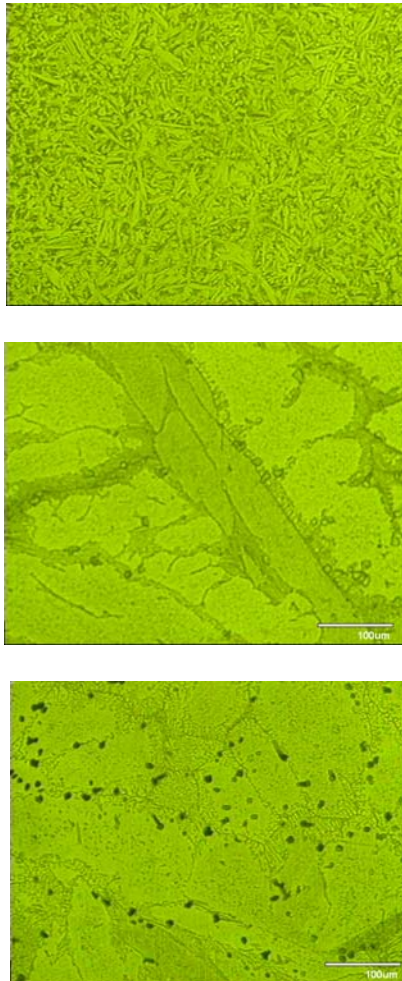


Figure 4B.5. Illustrates Fusion Weld Center Block Optical Microscopy for fracture specimens in Figure 4B.4.

C. FRICTION STIR PROCESSING

As indicated in Figure 3.1, tensile specimen blocks were also sectioned out of the single pass FSP region of this NAB material. These blocks were sectioned in the longitudinal direction of the FSP traverse, and the longitudinal mechanical properties for this region were determined and recorded. These data are summarized in the Appendix.

Figure 4C.1 provides optical microscopy and a montage for the transverse section of a single pass FSP through as-cast NAB. In the analysis of the OM, the four fundamental microstructures typical in the FSP of NAB and illustrated Figure 1.5 are apparent. The montage of the cross-section illustrates the shape of the stir zone. The advancing side is on the left and the retreating side is on the right. In region one, high in the stir zone, highly distorted and elongated primary α grains that are elongated in the horizontal sense. This distortion reflects the stirring action of the tool shoulder. Surrounding these primary α grains are dark-etching areas that are not resolved here, but are β transformation products. Regions two and three exhibit more equiaxed, fine grain structures with region three possessing the finer microstructure. Region four is similar to region one, but a decrease in the amount of deformation is apparent, where the distortion of primary α grains is less apparent. This region appears to be one of highly deformed base material and is likely representative of the TMAZ. The dark-etching in this region is a small fraction of β formed, probably due to the reversion of $\alpha + \kappa_{iii}$. The TMAZ extends down through the varying degrees of mechanical distortion and shares the lower portions of region five with the HAZ. The deformation in this region is small enough so that there is no break-up, refinement and homogenization of the grain structure as seen in the higher regions. Region six illustrates unprocessed base material.

Following the procedures outlined in the experimental procedures section, and as illustrated in Figure 1.5, tensile specimens were sectioned throughout the entire FSP region to determine the resulting distribution of mechanical properties. Figure 4C.2 illustrates the engineering stress vs engineering plastic strain for the center line alone. Additional data is provided in the Appendix. Ductility is highest in the high and middle regions of the stir zone. However, as the TMAZ and HAZ are approached at the bottom of the SZ (~8-9mm) the values for ductility decrease.

Figure 4C.3 illustrates a three dimensional representation of the tensile property results. Again, high ultimate tensile and yield strength values are observed as compared to base material. Yield strength values in FSP are higher than those attained in the fusion welding process, although strengthening is not as pronounced as in previous studies. This may reflect alloying and process history. The ultimate tensile strength of FSP and fusion welding are almost identical. The fluctuations in ductility for the FSP region are

not understood at this point. However, when Figure 4C.3 is compared to Figure 4B.3, it is evident that although ductility does fluctuate in the FSP region, it does not fall to low ductility values exhibited in the fusion weld.

Mechanical test data plotted along the center line of the single pass FSP stir zone is shown in Figure 4C.4. Ultimate tensile, yield strengths, and ductility are plotted as a function of depth in these figures. Also, SEM fractography is displayed for sample 5, and its neighboring samples (4 and 6). This was done to investigate the low ductility in this region. The SEM fractography illustrations also contain optical microscopy in sets of profiles of the failed tensile specimen, to allow examination of the associated fracture pattern. The profile pattern for the low ductility sample is very irregular, indicating a brittle fracture mode. This is consistent with the results found in section 4.B for the fusion weld. The low ductility region represented by sample 5, which corresponds to a location approximately 7.1mm(0.28in) below the surface in contact with the tool shoulder, and thus to the HAZ. Samples 4 and 6 SEM micrographs illustrate an increased amount of microvoid formation and coalescence, which is indicative of a more ductile failure mode. The microvoids are more apparent in sample 4 than in sample 6. However, both sample 4 and 6 SEM fractographs exhibit more ductile failure than sample 5, which exhibits cleavage cracking and a faceted appearance associated with a brittle failure mode.

Figure 4C.5 shows optical microscopy results. The prevalent feature of the microstructure for sample 4 (top), is elongated, highly distorted α grains with dark etching representing β transformation products in between the α grains. The morphology at this depth 4.6mm(0.18in), is representative of the bottom of the stir zone. Ductility in this region is 18%. The sample 6 represents ductility, approaches the nominal value for the base material. The prevalent grain structure here is representative of NAB base material. Sample 5 is the low ductility sample. The ductility is ~7.5%. The ductility and morphology illustrated by the OM, is indicative of the HAZ.

FSP 1Pass Optical Microscopy

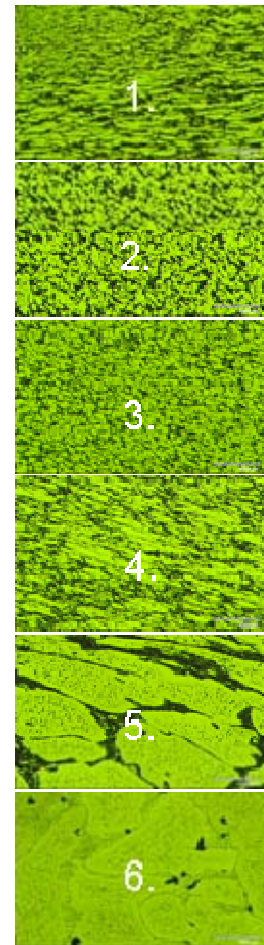
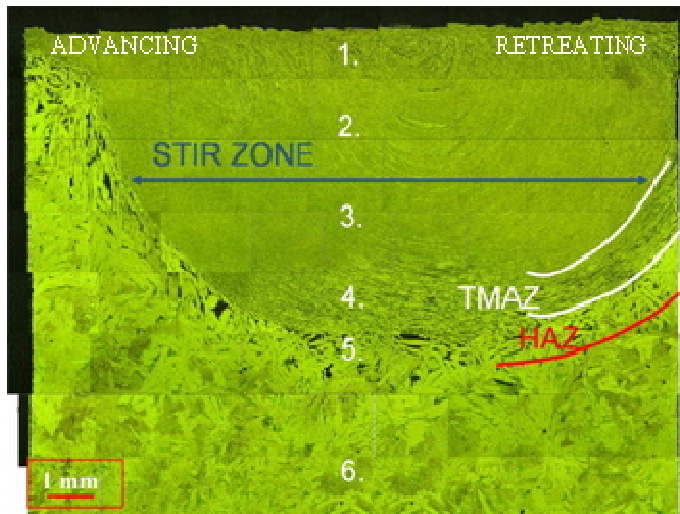


Figure 4C.1. Illustrates FSP 1Pass optical microscopy, delineating the process zones with a side row of montages taken at 370X.

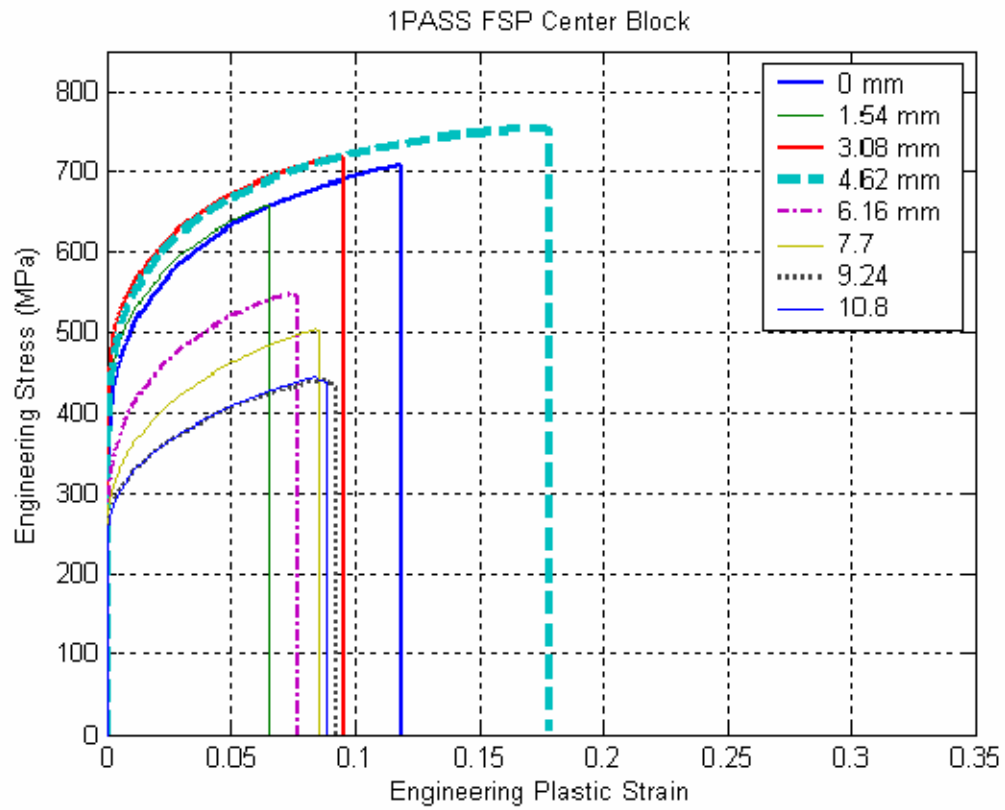


Figure 4C.2. Illustrates the Engineering Stress vs Engineering Plastic Strain for the center block of the single pass FSP portion of the NAB sample block.

FSP

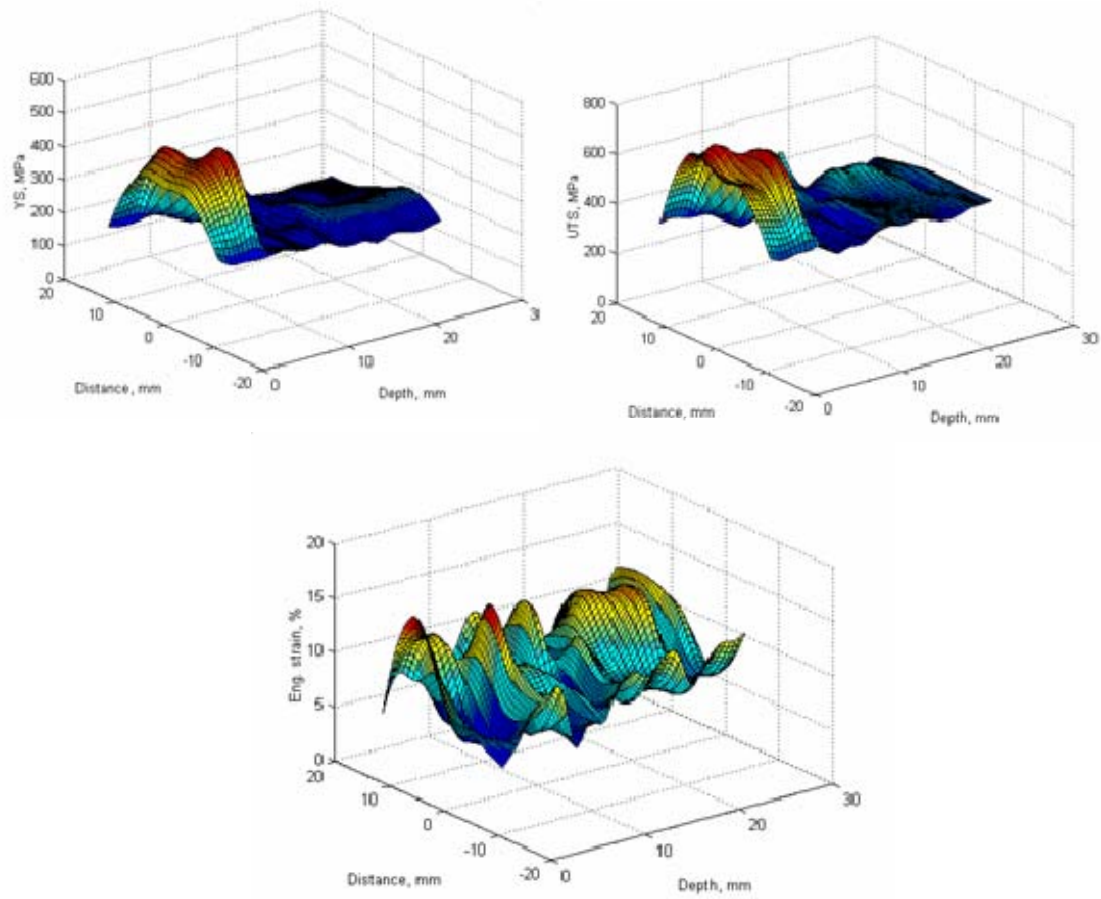


Figure 4C.3. Illustrates 3-dimensional mesh plots for ultimate tensile strength, yield strength and ductility for single pass FSP NAB material.

FSP 1 Pass SEM Fractography/Mechanical Properties

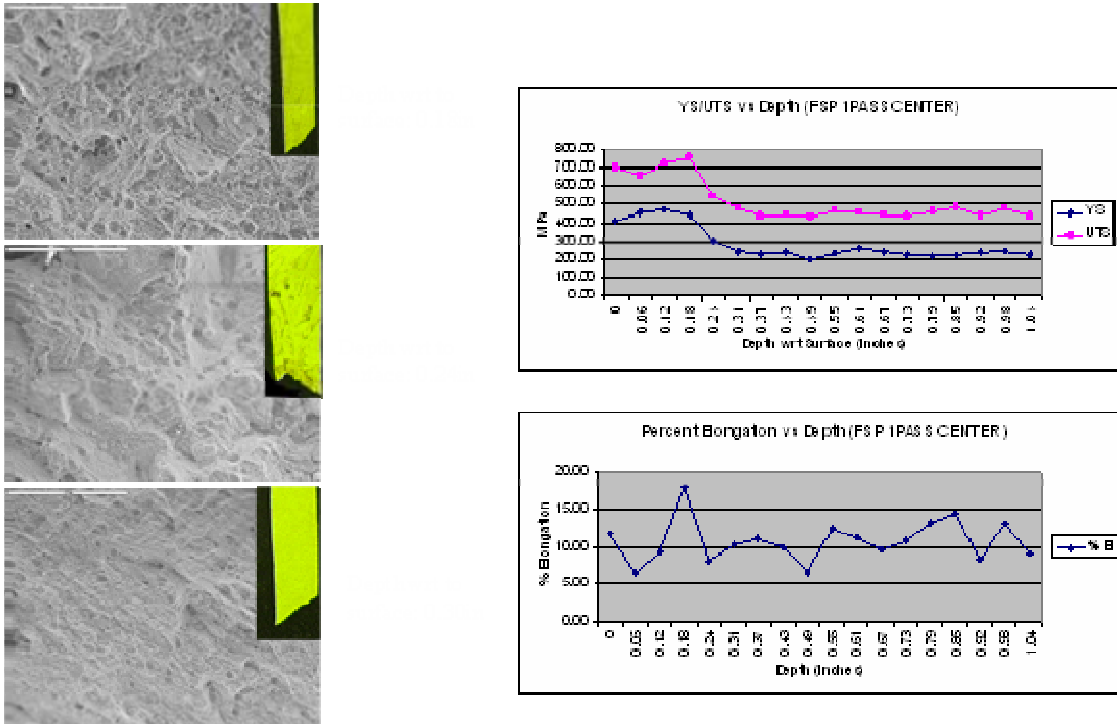


Figure 4C.4. Illustrates FSP 1 Pass Fractography and Mechanical Testing Data.

FSP 1Pass Optical Microscopy

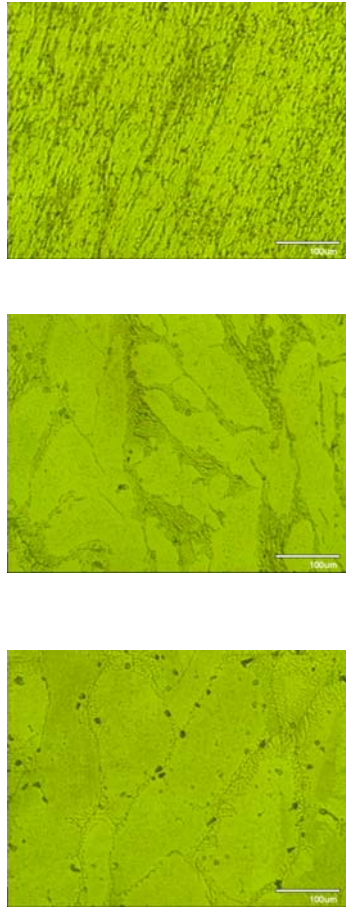


Figure 4C.5. Illustrates FSP 1Pass Center Block Optical Microscopy for fracture specimens in Figure 4C.4.

D. FSP 1PASS OVER FUSION WELD

The final section of the NAB plate examined here is the single-pass FSP over the fusion weld. The miniature tensile samples were sectioned from this region of the plate so that they were parallel to the axis of travel of the fusion weld and therefore perpendicular to the axis of travel for the single pass FSP.

Figure 4D.1 illustrates transverse view with respect to the FSP traversing direction. Thus, the FSP direction is out of the page and the welding direction is across the page. The illustration represents sectioning from a moderate ductility area in this

process region. Yield and ultimate strengths as well as ductility are plotted for this region in Figure 4D.2. There is a low ductility region located to the left of center (negative direction).

The SZ for this single pass FSP over fusion weld contains significant amounts of κ_{ii} and κ_{iii} particles. This implies that the peak temperatures reached here are not as high as those reached when NAB is subject to FSP alone. The montage illustrates a SZ, a TMAZ, and a HAZ that lies just below the SZ and TMAZ. Also apparent is that the fusion zone, which lies just below the first HAZ is followed by an additional HAZ prior to proceeding down into base material. In essence, because the tool pin depth of 6.2mm(.25 in) is not great enough to include the fusion zone and the second HAZ in the SZ for the FSP. As a result, as noted in Figure 4D.5, there are three low ductility regions that are crossed when proceeding from the processed surface of the plate to base material. The first low ductility region will be considered later. However, the second low ductility region is consistent with the FSP TMAZ/HAZ, and the third low ductility region appears to be due to the HAZ alone associated with the fusion weld.

Figure 4D.2 shows mesh plots illustrating the three dimensional mechanical property distribution for this process region. Comparable maximum strengths that are reached in processing over the fusion weld as opposed to FSP alone or fusion weld. Also, with the exception of the low ductility region that results to the left of center, the uniformity of property distribution seems to fall between that of FSP alone and FW. With the exception of the low ductility region, the uniformity of property distribution is greater than FW but less than FSP. The low ductility region was examined in greater detail and a cross-section was taken from this region. Optical microscopy was performed to determine the prevalent microstructures.

Figure 4D.3 illustrates the low ductility region traverse montage. Immediately apparent is the absence of process zones that are typical in fusion welds. At first, the absence of the fusion zone and additional HAZ would appear to have a positive effect on ductility distribution. However, with close observation of the microstructures in the montage, the presence of columnar dendritic structures is apparent in the upper right-hand corner (region 1). As this sample was repeatedly polished and observed with OM,

the dendritic structure would appear in variable volume fractions, but were consistently located in this region. Columnar dendrites are a result of solidification during rapid cooling at rates where, in alloys, the material deviates from planar solidification. This is important to note because the dendrites are not expected to be present in as-cast NAB material that has undergone equilibrium cooling. However, dendrites can form in NAB material that is adjacent to a multi-pass fusion weld (bordered on one side by cold metal). When FSP is then placed on top of this material, these dendrites may be drawn into the stir zone by the tool, without their complete homogenization on the retreating side.

Figure 4D.4 presents stress-strain curves illustrating the variation of ductility along the center line of this region. The low ductility that is present to the left of center also, seems to be reflected near the center. It is not until the region right-of-center that higher ductility values are witnessed. Figures 4D.6-4D.10 all illustrate the ductility values attained while transiting on the center block from the surface to base material. The SEM data are consistent with the mechanical test data in that a brittle fracture mode, indicated by cleavage cracking, is seen in increased amounts as ductility falls. The ductility in this area requires further testing and analysis.

FSP 1Pass over Fusion Weld Optical Microscopy

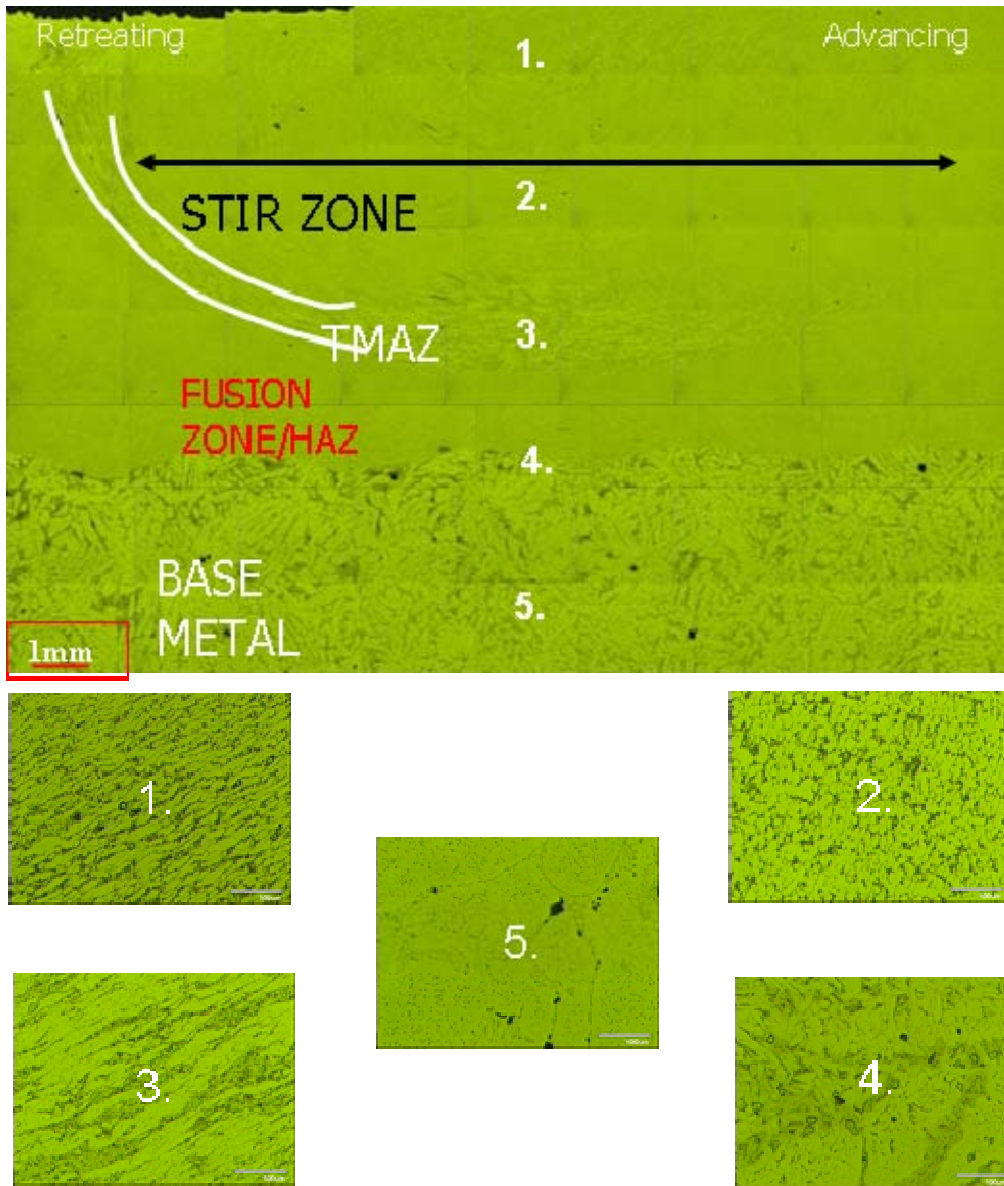


Figure 4D.1. Illustrates a montage of the cross-section view, with respect to FSP direction of the FSP 1 Pass over the Fusion Weld. This montage is taken from the moderate ductility region.

FSP over FW

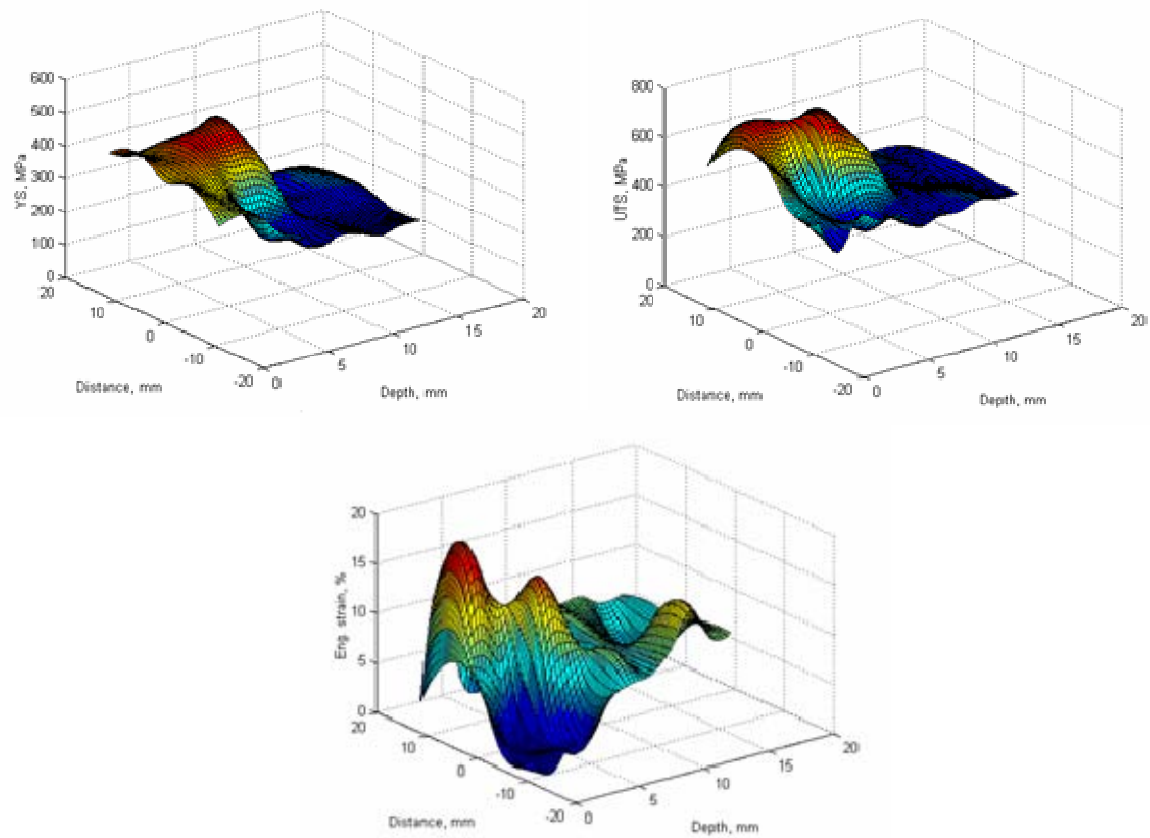


Figure 4D.2. Illustrates 3-dimensional mesh plots for ultimate tensile strength, yield strength and ductility for FSP 1Pass over Fusion Weld in NAB material.

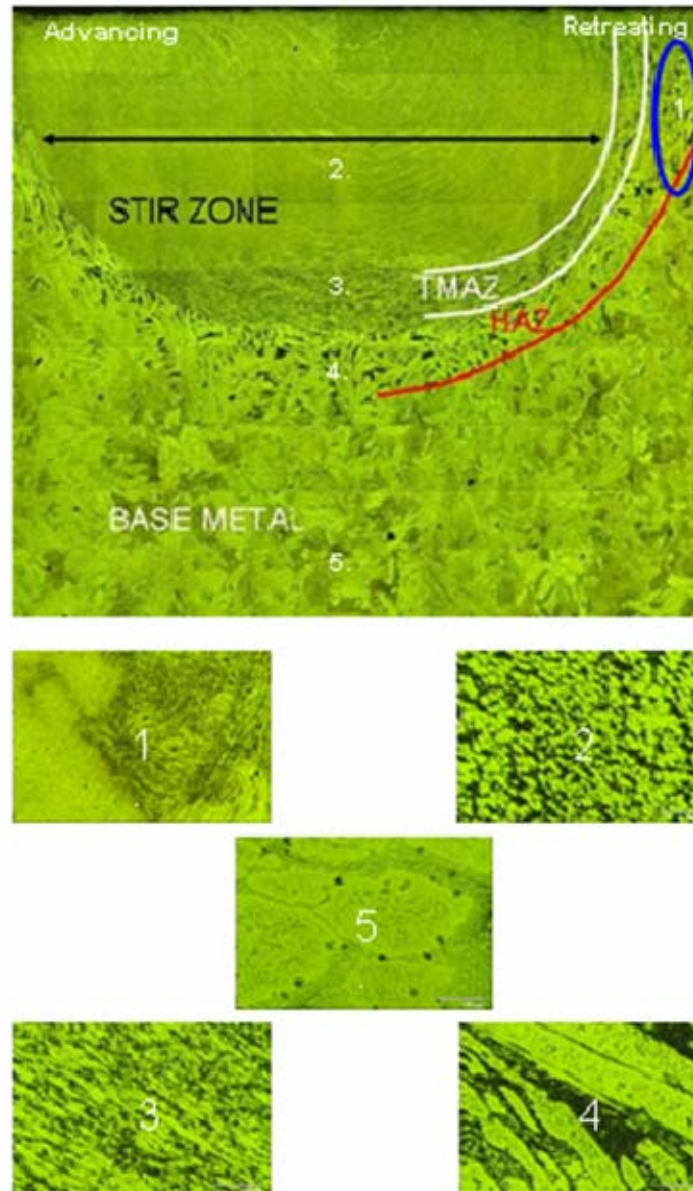


Figure 4D.3. Illustrates a montage of the cross-section view, with respect to FSP direction of the FSP 1 Pass over the Fusion Weld. This montage is taken from the low ductility region.

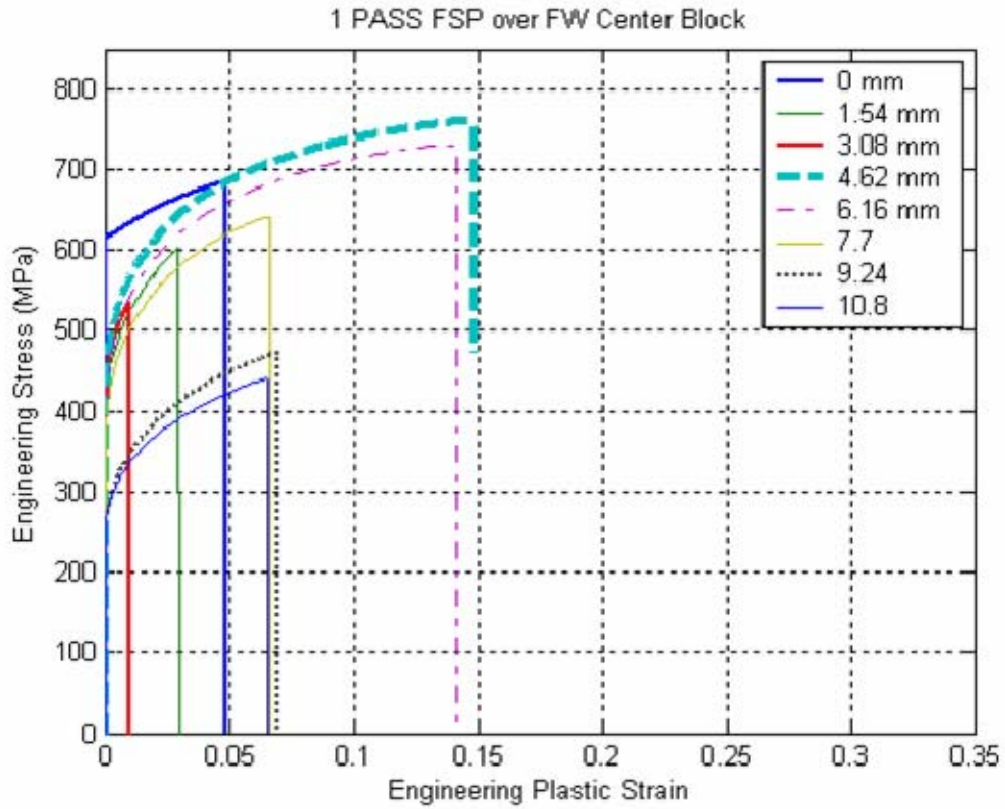


Figure 4D.4. Illustrates the Engineering Stress vs Engineering Plastic Strain for the center block of the single pass FSP over a Fusion Weld portion of the NAB sample block.

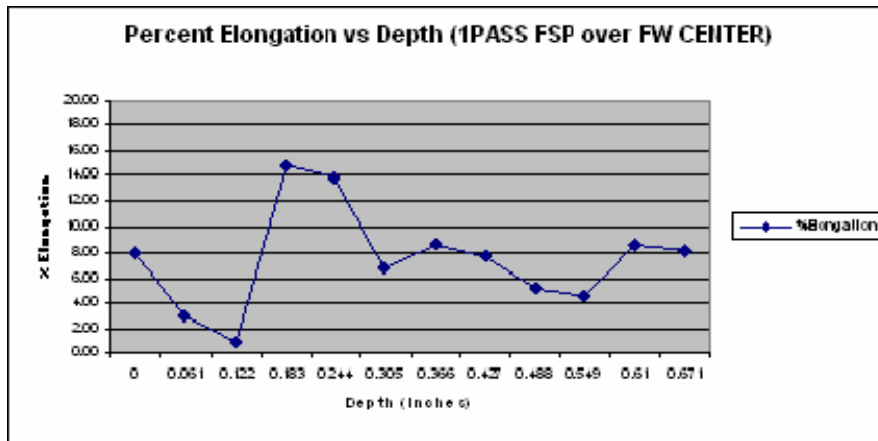
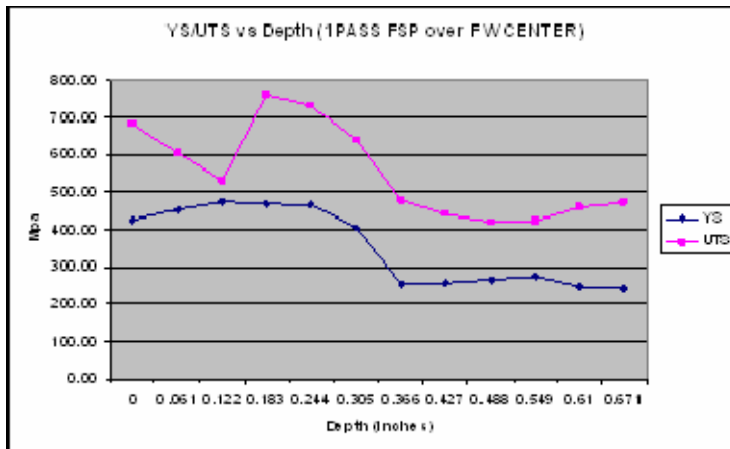


Figure 4D.5. Illustrates FSP 1Pass over Fusion Weld mechanical properties vs depth from the NAB material surface. This data represents the center block only. Additional data is available in Appendix A.

FSP 1Pass over FW SEM Fractography and Ductility Data - Sample #1

Sample No: 1

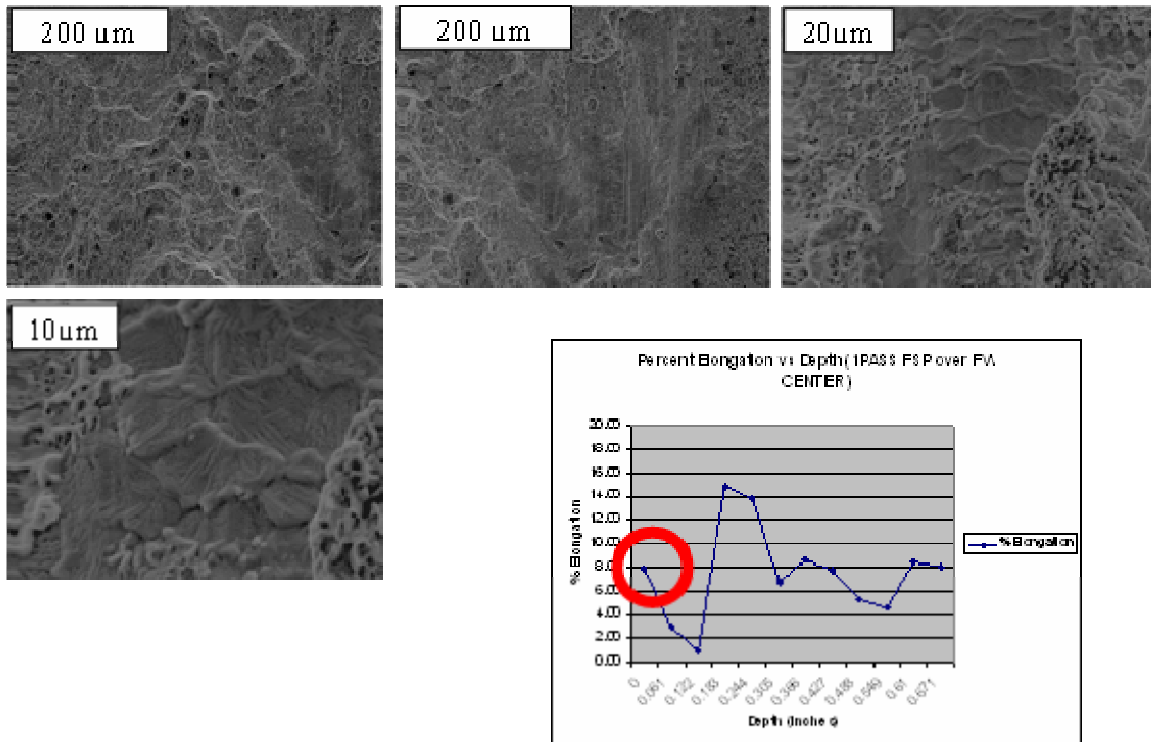


Figure 4D.6. Illustrates FSP 1 Pass over SEM Fractography and ductility data for the surface specimen (sample #1) sectioned from the center block.

FSP 1Pass over FW SEM Fractography and Ductility Data - Sample #3

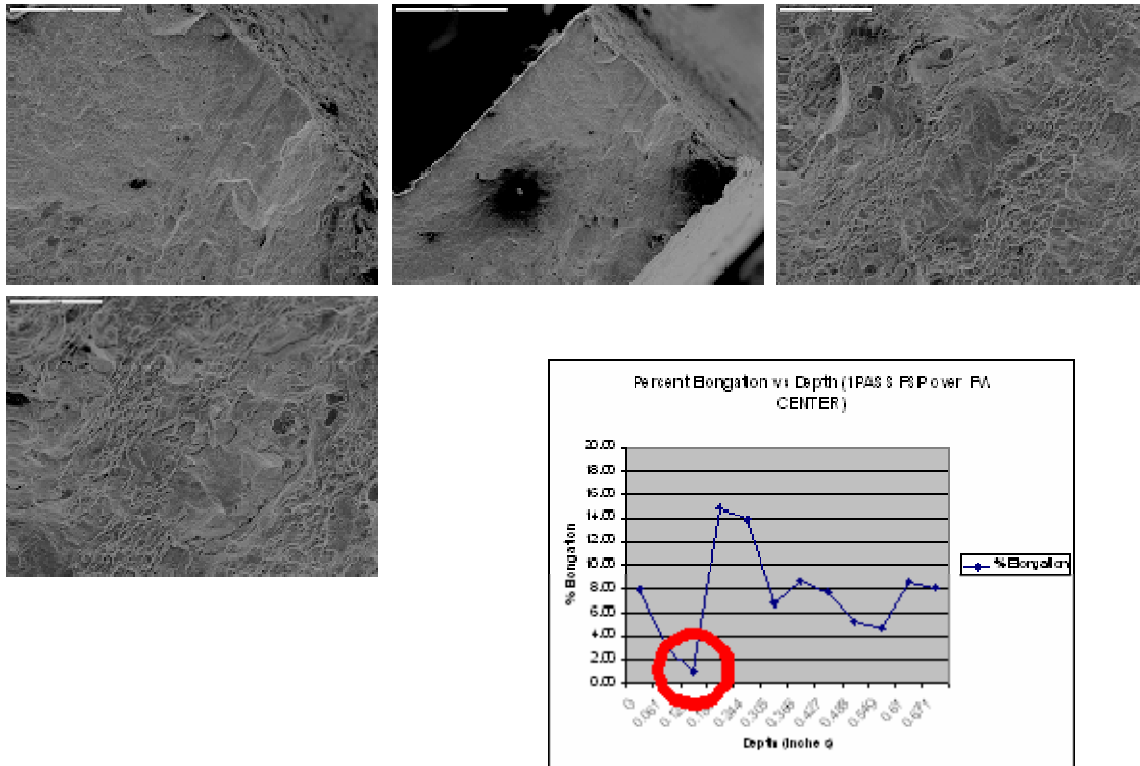


Figure 4D.7. Illustrates FSP 1 Pass over SEM Fractography and ductility data for the lowest ductility specimen (sample #3) sectioned from the center block.

FSP 1Pass over FW SEM Fractography and Ductility Data - Sample #5

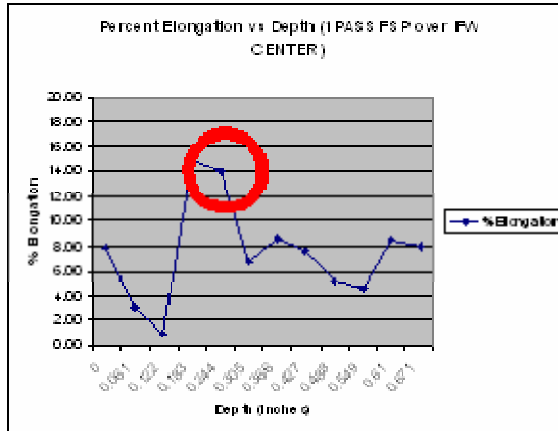
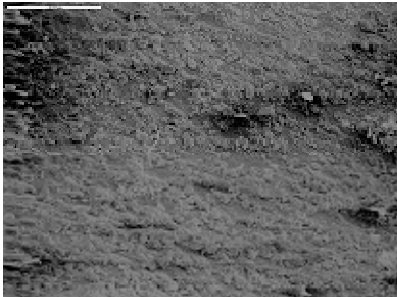
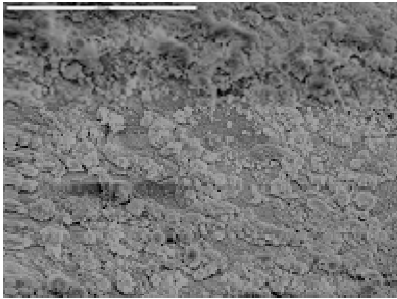


Figure 4D.8. Illustrates FSP 1 Pass over SEM Fractography and ductility data for a high ductility specimen (sample #5) sectioned from the center block.

FSP 1Pass over FW SEM Fractography and Ductility Data - Sample #6

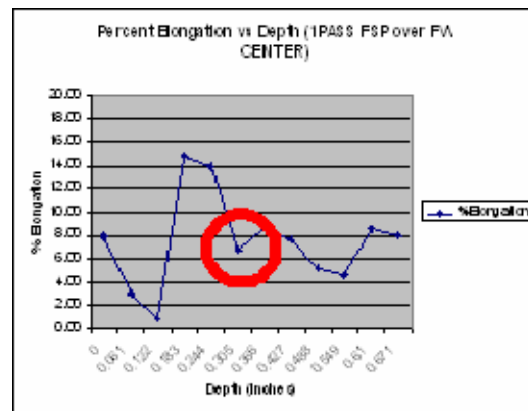


Figure 4D.9. Illustrates FSP 1 Pass over SEM Fractography and ductility data for a low ductility specimen (sample #6) sectioned from the center block. Note that this samples location corresponds to the HAZ effect seen in other process.

FSP 1Pass over FW SEM Fractography and Ductility Data - Sample #7

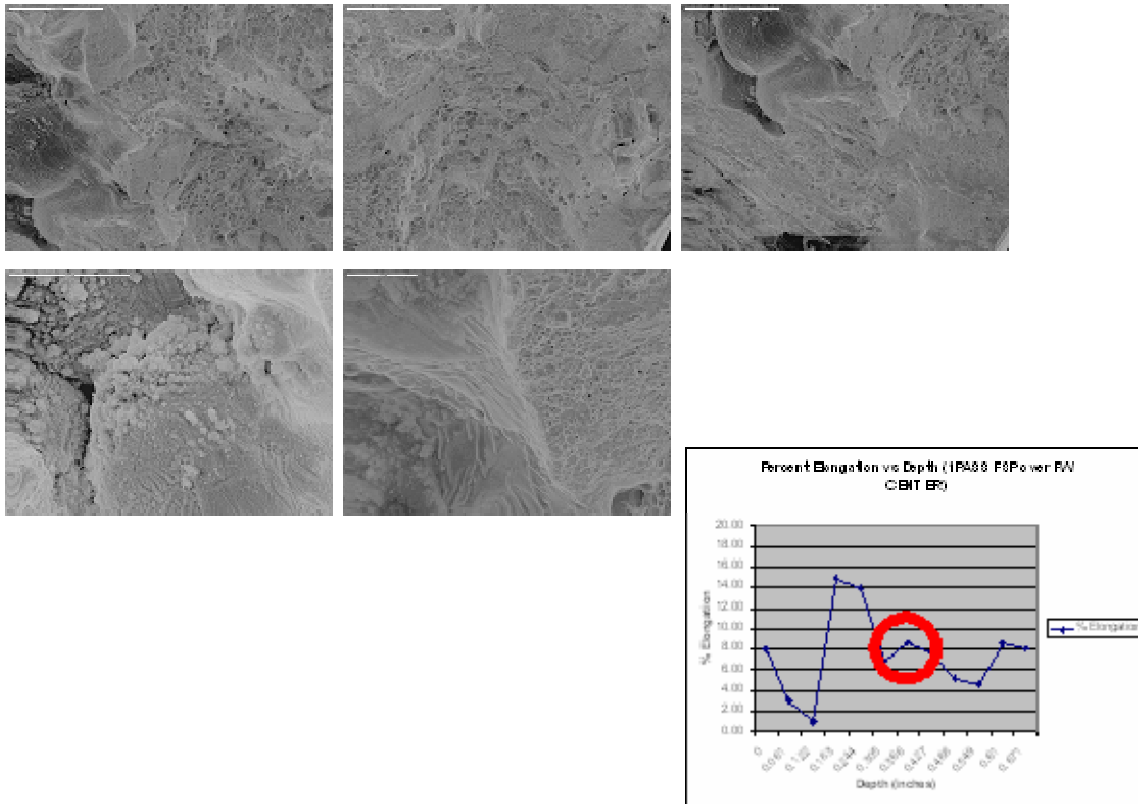


Figure 4D.10. Illustrates FSP 1 Pass over SEM Fractography and ductility data for a moderate ductility specimen (sample #7) sectioned from the center block.

THIS PAGE INTENTIONALLY LEFT BLANK

V. CONCLUSIONS AND RECOMMENDATIONS

A. CONCLUSIONS

■Annealing studies identify the effects of elevated temperature at the S/L interface as a direct contributor to the reduction in ductility- HAZ affect. Beta transformation products play a significant role.

Although ductility results in FSP 1Pass are erratic and low in the TMAZ/HAZ, they are not consistently low, nor do they achieve the lower values experienced in the HAZ of the Fusion Weld.

When utilizing FSP 1Pass over FW, where both the SZ and fusion zone are present, at least two regions of low ductility will result as you progress from the surface of the material through the process zones.

The presence of dendritic structures were recorded in the 'FSP 1Pass over FW' montages. (These brittle microstructures may be contributory to regions of low ductility at the FSP/FW/Base Metal interface.)

B. RECOMMENDATIONS

■Research the affects of cooling rates on ductility of NAB material, and relate to those experienced in the HAZ. If a significant portion of the low ductility lies with excessive cool-down rates, pre-heating may solve this problem. (May also create coarser grain structures and reduce mechanical properties)

Isolate the origin of brittle structures observed in FSP 1Pass over FW montages.
If from FW metal: recommend using multi-pass patterns to fully encompass the fusion weld in the friction stir processed zone.

Continue research on the multi-pas FSP over FW section of the NAB plate. Multi-pass FSP is more practical in fleet application.

THIS PAGE INTENTIONALLY LEFT BLANK

APPENDIX

Base metal						
File	W	Th	YS	UTS	EI	
1_1	1.82	0.97	184.60	421.70	11.90	
1_12	1.85	0.95	186.66	402.20	9.53	
1_24	1.79	0.95	221.91	420.32	9.49	
2_2	1.99	0.93	242.60	426.32	9.37	
2_13	1.93	0.81	203.95	401.71	8.96	
2_23	1.89	0.81	208.99	396.85	7.62	
		MPa	208.12	411.51	9.48	
		±	21.96	12.64	1.39	
		ksi	30.18	59.68		
		±	3.18	1.83		

Heat Treatment													
		Air Cooling					Water quenching						
T, °C	File	W	Th	YS	UTS	EI	File	W	Th	YS	UTS	EI	
	2_1	1.93	0.98	174.58	427.50	12.19	1_2	1.84	0.97	206.85	423.78	8.30	
800	2_14	1.89	0.92	184.83	468.59	13.79	1_11	1.84	0.91	183.34	452.59	12.44	
	2_24	1.90	0.97	184.17	412.59	9.12	1_23	1.81	0.97	187.18	430.61	10.90	
			MPa	181.19	436.23	11.70			MPa	192.46	435.66	10.54	
			±	5.73	29.01	2.37			±	12.61	15.05	2.09	
			ksi	26.28	63.27				ksi	27.91	63.18		
			±	0.83	4.21				±	1.83	2.18		
T, °C	File	W	Th	YS	UTS	EI	File	W	Th	YS	UTS	EI	
	1_3	1.84	0.97	191.63	452.46	12.07	1_5	1.84	0.99	168.91	414.63	10.39	
850	1_14	1.86	0.97	196.17	429.33	10.19	1_10	1.85	0.97	173.42	440.43	12.57	
	1_21	1.84	0.95	191.88	430.10	11.13	1_20	1.84	0.97	167.10	419.01	11.07	
			MPa	193.23	437.29	11.13			MPa	169.81	424.69	11.34	
			±	2.55	13.14	0.94			±	3.25	13.80	1.12	
			ksi	28.02	63.42				ksi	24.63	61.59		
			±	0.37	1.91				±	0.47	2.00		

T, °C	File	W	Th	YS	UTS	EI	File	W	Th	YS	UTS	EI
	1_6	1.87	0.96	235.12	423.55	6.04	1_7	1.85	0.90	172.62	424.49	7.73
900	1_15	1.85	0.91	232.81	435.09	7.13	1_16	1.85	0.93	155.28	418.73	8.08
	1_19	1.85	0.95	248.77	457.16	6.70	1_18	1.85	0.91	162.28	407.61	8.86
			MPa	238.90	438.60	6.63			MPa	163.39	416.95	8.22
			±	8.63	17.08	0.55			±	8.72	8.58	0.58
			ksi	34.65	63.61				ksi	23.70	60.47	
			±	1.25	2.48				±	1.27	1.24	
T, °C	File	W	Th	YS	UTS	EI	File	W	Th	YS	UTS	EI
	2_3	2.00	0.93	260.08	432.14	5.04						
950	2_10	1.95	0.98	251.87	474.50	6.78	2_11	2.00	0.95	179.76	416.35	6.48
	2_22	1.94	0.67	254.62	424.72	3.51	2_21			170.22	415.42	6.44
			MPa	255.53	443.78	5.11			MPa	174.99	415.89	6.46
			±	4.18	26.86	1.63			±	6.75	0.66	0.03
			ksi	37.06	64.36				ksi	25.38	60.32	
			±	0.61	3.89				±	0.98	0.10	
T, °C	File	W	Th	YS	UTS	EI	File	W	Th	YS	UTS	EI
	2_5	2.00					2_6	1.95	0.95	204.39	451.31	6.35
1000	2_12	1.90	0.87	266.04	469.14	4.96	2_14	1.95	0.93	234.59	490.74	5.62
	2_20	1.99	0.91	271.54	494.38	4.53	2_19	1.90	0.92	202.65	500.34	8.67
			MPa	268.79	481.76	4.74			MPa	213.88	480.80	6.88
			±	3.89	17.85	0.30			±	17.96	25.98	1.59
			ksi	38.98	69.87				ksi	31.02	69.73	
			±	0.56	2.59				±	2.60	3.77	
Inches	File	W	Th	YS	UTS	EI		mm				
0	F0-1	1.76	0.93	410.99	706.97	11.78		0				
0.061	F0-2	1.79	0.95	454.33	658.22	6.51		1.54				
0.122	F0-3	1.77	0.97	472.99	718.61	9.44		3.08				
0.183	F0-4	1.77	0.96	447.87	752.74	17.87		4.62				
0.244	F0-5	1.79	0.97	302.98	547.45	8.00		6.16				
0.305	F0-6	1.80	0.97	239.66	477.41	10.33		7.7				
0.366	F0-7	1.80	0.92	230.66	442.17	11.05		9.24				
0.427	F0-8	1.80	0.95	236.62	445.43	10.00		10.8				

0.488	F0-9	1.78	0.93	199.01	434.33	6.63	12.3				
0.549	F010	1.80	0.88	232.19	469.29	12.47	13.9				
0.61	F011	1.81	0.86	258.46	458.22	11.22	15.4				
0.671	F012	1.79	0.92	244.41	447.84	9.61	16.9				
0.732	F013	1.80	0.91	224.22	441.87	10.82	18.5				
0.793	F014	1.79	0.93	222.18	463.96	13.26	20				
0.854	F015	1.77	0.95	225.87	483.16	14.44	21.6				
0.915	F016	1.78	0.93	236.70	437.42	8.30	23.1				
0.976	F017	1.77	0.95	239.75	479.82	13.04	24.6				
1.037	F018	1.80	0.93	223.33	439.26	9.17	26.2				
				MPa	283.46	516.90	10.77				
				±	92.64	110.13	2.82				
				ksi	41.11	74.97					
				±	13.44	15.97					
T, °C	File	W	Th	YS	UTS	EI	mm				
0	F1-1	1.68	0.96	400.54	729.69	16.55	0				
0.061	F1-2	1.71	0.97	441.87	717.75	13.84	1.54				
0.122	F1-3	1.71	0.97	462.51	731.15	13.70	3.08				
0.183	F1-4	1.73	0.97	305.71	532.26	6.34	4.62				
0.244	F1-5	1.75	0.97	228.97	389.41	5.23	6.16				
0.305	F1-6	1.74	0.97	231.91	427.84	8.98	7.7				
0.366	F1-7	1.73	0.97	232.12	441.10	9.96	9.24				
0.427	F1-8	1.73	0.96	236.69	450.34	9.73	10.8				
0.488	F1-9	1.76	0.97	222.65	488.86	15.32	12.3				
0.549	F110	1.73	0.84	235.82	415.57	7.12	13.9				
0.61	F111	1.73	0.84	219.71	453.53	10.42	15.4				
0.671	F112	1.70	0.89	233.16	513.12	13.11	16.9				
0.732	F113	1.70	1.24	197.63	497.76	14.63	18.5				
0.793	F114	1.70	0.92	221.52	510.31	13.90	20				
0.854	F115	1.73	0.96	211.15	469.33	13.91	21.6				
0.915	F116	1.73	0.95	205.94	460.98	11.47	23.1				

0.976	F117	1.73	0.96	203.70	466.90	14.55	24.6				
1.037	F118	1.75	0.93	191.32	426.62	8.58	26.2				
			MPa	260.16	506.81	11.52					
			±	84.68	107.33	3.35					
			ksi	37.73	73.50						
			±	12.28	15.57						
T, °C	File	W	Th	YS	UTS	EI					
0	F2-1	1.42	0.93	219.26	406.24	6.51					
0.061	F2-2	1.40	0.99	209.77	413.82	9.71	1.54				
0.122	F2-3	1.43	0.95	211.09	398.87	8.80	3.08				
0.183	F2-4	1.39	0.93	217.97	392.99	8.12	4.62				
0.244	F2-5	1.39	0.93	225.27	410.93	8.43	6.16				
0.305	F2-6			218	435.00	10.50	7.7				
0.366	F2-7	1.40	0.99	211.85	458.30	13.42	9.24				
0.427	F2-8	1.39	0.96	209.59	438.61	12.40	10.8				
0.488	F2-9	1.39	0.63	208.47	391.06	7.49	12.3				
0.549	F210	1.42	0.92	280.23	569.02	12.48	13.9				
0.61	F211	1.39	0.96	186.69	392.21	10.06	15.4				
0.671	F212	1.39	0.76	194.17	368.40	6.92	16.9				
0.732	F213	1.39	0.82	187.11	410.58	10.92	18.5				
0.793	F214	1.37	0.95	185.34	361.82	6.80	20				
0.854	F215	1.38	0.92	190.02	382.83	8.36	21.6				
0.915	F216	1.34	0.95	189.85	400.59	9.57	23.1				
0.976	F217	1.34	0.93	186.82	435.69	14.05	24.6				
1.037	F218	1.34	0.90	192.77	412.89	9.96	26.2				
			MPa	206.90	415.55	9.69					
			±	22.72	45.49	2.28					
			ksi	30.01	60.27						
			±	3.30	6.60						
0	F-1-1	1.39	0.91	399.26	681.83	8.32					
0.061	F-1-2	1.40	0.93	443.47	666.86	7.57	1.54				
0.122	F-1-3	1.43	0.97	457.12	653.92	6.34	3.08				

0.183	F-1-4	1.06	0.73	516.30	755.18	13.39	4.62				
0.244	F-1-5	1.21	0.9	280.97	491.96	6.86	6.16				
0.305	F-1-6	1.2	0.91	222.24	417.11	7.96	7.7				
0.366	F-1-7	1.16	0.91	235.18	423.97	7.2	9.24				
0.427	F-1-8	1.16	0.9	223.03	449.94	9.94	10.8				
0.488	F-1-9	1.28	0.95	241.58	391.5	5.84	12.3				
0.549	F-1-10	1.21	0.91	246.27	460.83	10.17	13.9				
0.61	F-1-11	1.21	0.7	261.52	455.2	7.54	15.4				
0.671	F-1-12			262	455	8					
0.732	F-1-13			262	455	8					
0.793	F-1-14			262	455	8					
0.854	F-1-15			262	455	8					
0.915	F-1-16			262	455	8					
0.976	F-1-17			262	455	8					
1.037	F-1-18			262	455	8					
				MPa	297.83	501.85	8.17				
				±	89.52	106.93	1.66				
				ksi	43.20	72.78					
				±	12.98	15.51					
0	F-2-1	1.72	0.88	269.14	464.30	6.45	0				
0.061	F-2-2	1.72	0.93	241.30	442.95	8.10	1.54				
0.122	F-2-3	1.72	0.96	240.16	456.09	10.70	3.08				
0.183	F-2-4	1.73	0.96	235.35	454.86	11.45	4.62				
0.244	F-2-5	1.72	0.96	238.79	468.94	12.36	6.16				
0.305	F-2-6	1.72	0.96	244.54	412.19	6.51	7.7				
0.366	F-2-7	1.73	0.96	230.54	425.81	8.52	9.24				
0.427	F-2-8	1.72	0.95	227.48	423.62	8.05	10.8				
0.488	F-2-9	1.72	0.95	234.83	455.74	11.19	12.3				
0.549	F-2-10	1.72	0.95	213.46	467.40	12.00	13.9				
0.61	F-2-11	1.72	0.96	204.75	456.93	11.10	15.4				
0.671	F-2-12	1.72	0.97	206.51	463.81	12.49	16.9				
0.732	F-2-13	1.75	0.97	191.62	448.81	12.76	18.5				

0.793	F-2-14	1.72	0.99	209.15	429.94	9.23	20				
0.854	F-2-15	1.75	0.99	201.85	432.82	11.12	21.6				
0.915	F-2-16	1.75	0.97	193.13	452.33	12.44	23.1				
0.976	F-2-17	1.73	0.96	201.95	452.41	12.31	24.6				
1.037	F-2-18	1.75	0.95	207.90	462.26	13.23	26.2				
				MPa	221.80	448.40	10.56				
				±	21.28	16.76	2.18				
				ksi	32.17	65.03					
				±	3.09	2.43					
0	W0-1	1.70	0.90	339.16	732.44	16.43					
0.061	W0-2	1.70	0.90	336.33	714.17	16.74	1.54				
0.122	W0-3	1.71	0.85	378.58	711.12	18.63	3.08				
0.183	W0-4	1.71	0.90	390.17	700.40	15.07	4.62				
0.244	W0-5	1.73	0.88	423.01	722.27	18.00	6.16				
0.305	W0-6	1.72	0.86	416.36	712.34	9.26	7.7				
0.366	W0-7	1.73	0.87	360.97	520.02	3.90	9.24				
0.427	W0-8	1.73	1.04	286.90	416.52	4.45	10.8				
0.488	W0-9	1.75	0.95	275.56	439.12	5.97	12.3				
0.549	W010	1.73	0.93	289.56	463.50	7.91	13.9				
0.61	W011	1.76	0.96	245.55	438.45	8.53	15.4				
0.671	W012	1.79	0.92	218.32	429.46	8.33	16.9				
0.732	W013	1.74	0.94	199.79	411.16	7.00	18.5				
0.793	W014	1.73	0.97	224.74	392.93	6.01	20				
0.854	W015	1.76	0.97	220.02	436.85	9.58	21.6				
				MPa	307.00	549.38	10.39				
				±	76.27	143.19	5.13				
				ksi	44.53	79.68					
				±	11.06	20.77					

0	W-1-1	1.70	0.96	323.39	720.28	17.53	0				
0.061	W-1-2	1.70	0.90	372.16	710.26	14.29	1.54				
0.122	W-1-3	1.70	0.91	385.79	554.09	2.70	3.08				
0.183	W-1-4	1.70	0.91	238.25	463.20	5.63	4.62				
0.244	W-1-5	1.72	0.91	285.19	375.51	2.45	6.16				
0.305	W-1-6	1.72	0.92	282.13	441.86	5.75	7.7				
0.366	W-1-7	1.72	0.93	266.26	445.14	6.51	9.24				
0.427	W-1-8	1.76	0.95	267.00	451.86	7.60	10.8				
0.488	W-1-9	1.75	0.95	249.44	426.68	7.31	12.3				
0.549	W-10	1.77	0.58	248.61	450.07	6.45	13.9				
0.61	W-11			226.00	445.00	8.00	15.4				
0.671	W-12	1.76	0.93	206.32	438.80	9.57	16.9				
0.732	W-13	1.77	0.96	193.18	406.76	8.82	18.5				
0.793	W-14	1.75	0.92	198.23	407.58	7.80	20				
0.854	W-15	1.77	0.90	213.44	385.60	6.13	21.6				

MPa	263.69	474.85	7.77
±	58.94	105.79	3.88
ksi	38.24	68.87	
±	8.55	15.34	

0	W-2-1			360	500	3.00	0				
0.061	W-2-2	1.75	0.88	355.14	502.47	2.48	1.54				
0.122	W-2-3	1.79	0.87	334.12	496.95	2.65	3.08				
0.183	W-2-4	1.77	0.92	261.73	428.41	5.33	4.62				
0.244	W-2-5	1.80	0.86	250.34	458.66	8.23	6.16				
0.305	W-2-6	1.79	0.91	235.23	405.21	5.46	7.7				
0.366	W-2-7	1.77	0.95	232.32	423.24	7.71	9.24				
0.427	W-2-8	1.81	0.92	218.70	398.23	6.96	10.8				
0.488	W-2-9	1.80	0.91	205.75	428.17	9.04	12.3				
0.549	W-10	1.81	0.52	196.53	400.75	7.61	13.9				
0.61	W-11			199.00	400.00	7.00	15.4				

0.671	W-12	1.80	0.87	201.61	398.43	6.12	16.9
0.732	W-13	1.81	0.91	211.11	414.22	8.10	18.5
0.793	W-14	1.79	0.87	228.21	460.51	10.31	20
0.854	W-15	1.81	0.87	192.53	381.96	6.38	21.6

MPa	237.31	428.37	6.67
±	50.06	37.66	2.20
ksi	34.42	62.13	
±	7.26	5.46	

0	W-3-1	1.70	0.92	247.15	441.93	8.24	0
0.061	W-3-2	1.72	0.91	235.66	445.62	7.91	1.54
0.122	W-3-3	1.72	0.96	227.35	415.84	7.15	3.08
0.183	W-3-4	1.73	0.91	223.04	437.53	9.26	4.62
0.244	W-3-5	1.75	0.90	210.83	413.96	8.49	6.16
0.305	W-3-6	1.75	0.90	205.38	402.74	6.88	7.7
0.366	W-3-7	1.77	0.91	214.09	352.29	4.12	9.24
0.427	W-3-8	1.75	0.87	207.37	435.94	8.92	10.8
0.488	W-3-9	1.77	0.86	202.49	417.87	8.42	12.3
0.549	W-10	1.75	0.48	217.70	369.23	4.85	13.9
0.61	W-11			207	369.00	5.85	15.4
0.671	W-12	1.77	0.93	197.78	368.68	6.85	16.9
0.732	W-13	1.77	0.91	189.57	365.76	6.71	18.5
0.793	W-14	1.77	0.86	202.97	430.10	10.55	20
0.854	W-15	1.76	0.85	192.85	392.15	6.67	21.6

Bad Specimen

MPa	212.08	403.91	7.39
±	15.87	32.06	1.69
ksi	30.76	58.58	
±	2.30	4.65	

0	W1-1	1.75	0.86	367.16	702.42	13.34	0				
0.061	W1-2	1.71	0.86	352.88	723.68	14.96	1.54				
0.122	W1-3	1.73	0.85	372.20	629.00	5.49	3.08				
0.183	W1-4	1.71	0.92	382.98	719.13	14.70	4.62				
0.244	W1-5	1.71	0.92	419.95	716.67	12.18	6.16				
0.305	W1-6	1.72	0.92	475.45	760.59	14.43	7.7				
0.366	W1-7	1.72	0.93	343.55	521.40	4.20	9.24				
0.427	W1-8	1.80	0.95	279.23	411.15	4.98	10.8				
0.488	W1-9	1.72	1.00	296.63	456.69	6.64	12.3				
0.549	W1-10	1.73	0.95	285.38	429.67	4.80	13.9				
0.61	W1-11	1.71	1.00	222.07	427.80	6.04	15.4				
0.671	W1-12	1.72	0.99	242.43	406.70	5.24	16.9				
0.732	W1-13	1.72	0.99	245.53	450.69	9.61	18.5				
0.793	W1-14	1.73	0.98	225.78	388.96	5.28	20				
0.854	W1-15	1.75	0.99	220.92	438.04	9.43	21.6				

MPa	315.48	545.51	8.75
±	79.13	143.22	4.12
ksi	45.75	79.12	
±	11.48	20.77	

0	W2-1			360.0	700.0	10.0	0				
0.061	W2-2	1.76	0.82	358.28	706.07	9.69	1.54				
0.122	W2-3	1.77	0.76	320.81	442.49	1.30	3.08				
0.183	W2-4	1.77	0.87	241.8	408.73	4.45	4.62				
0.244	W2-5	1.79	0.87	250.09	428.36	6.90	6.16				
0.305	W2-6	1.77	0.92	284.05	398.94	4.00	7.7				
0.366	W2-7	1.79	0.91	270.45	434.67	7.19	9.24				
0.427	W2-8	1.79	1.00	244.50	401.70	5.23	10.8				
0.488	W2-9	1.76	0.97	227.14	418.39	6.00	12.3				

0.549	W-10	1.76	0.95	196.35	390.61	5.68	13.9
0.61	W-11	1.77	0.97	226.08	437.79	9.36	15.4
0.671	W-12	1.79	0.95	210.06	381.14	5.88	16.9
0.732	W-13	1.79	1.00	233.57	428.73	9.69	18.5
0.793	W-14	1.79	1.00	196.99	433.00	10.11	20
0.854	W-15	1.79	1.00	211.75	440.95	11.75	21.6

MPa	247.99	439.40	6.95
±	46.80	79.25	2.87
ksi	35.97	63.73	
±	6.79	11.49	

0	W3-1	1.72	0.92	255.68	412.60	5.23	0
0.061	W3-2	1.75	0.91	245.53	414.16	7.64	1.54
0.122	W3-3	1.73	0.90	271.54	494.38	4.53	3.08
0.183	W3-4			255.00	450.00	6.00	4.62
0.244	W3-5	1.75	0.87	243.00	418.11	7.30	6.16
0.305	W3-6	1.76	0.87	216.18	428.32	9.60	7.7
0.366	W3-7	1.77	0.85	206.87	423.91	9.30	9.24
0.427	W3-8	1.76	0.82	201.21	444.70	11.54	10.8
0.488	W3-9	1.76	0.87	212.65	408.85	7.85	12.3
0.549	W-10	1.77	0.82	180.03	405.16	8.70	13.9
0.61	W-11	1.77	0.80	193.20	396.40	9.04	15.4
0.671	W-12	1.75	0.93	202.99	419.98	8.72	16.9
0.732	W-13	1.77	0.85	190.63	418.02	9.98	18.5
0.793	W-14	1.77	0.92	183.96	402.22	9.43	20
0.854	W-15	1.77	0.88	193.60	394.24	7.22	21.6

MPa	216.80	422.07	8.14
±	29.57	25.41	1.88
ksi	31.44	61.21	
±	4.29	3.69	

0	1PW-1	1.67	1.11	426.37	683.02	7.95	0
0.061	1PW-2	1.67	0.96	452.39	603.06	2.98	1.54
0.122	1PW-3	1.71	0.93	473.46	532.46	0.99	3.08
0.183	1PW-4	1.72	0.93	468.17	759.76	14.89	4.62
0.244	1PW-5	1.71	0.93	466.40	730.23	13.90	6.16
0.305	1PW-6	1.72	0.92	403.29	640.31	6.77	7.7
0.366	1PW-7	1.71	0.97	254.64	476.48	8.66	9.24
0.427	1PW-8	1.72	0.96	256.84	440.24	7.68	10.8
0.488	1PW-9	1.76	0.92	265.36	421.08	5.23	12.3
0.549	1PW-10	1.75	0.96	273.89	422.69	4.59	13.9
0.61	1PW-11	1.74	0.96	247.47	458.06	8.54	15.4
0.671	1PW-12	1.76	1.00	242.58	471.81	8.05	16.9

MPa	352.57	553.27	7.52
±	102.08	124.38	3.99
ksi	51.13	80.24	
±	14.80	18.04	

0	1PW-1	1.72	1.00	477.28	688.10	8.26	0
0.061	1PW-2	1.72	0.96	446.46	745.17	18.53	1.54
0.122	1PW-3	1.72	0.95	483.35	743.77	14.38	3.08
0.183	1PW-4	1.75	0.96	502.82	741.51	11.74	4.62
0.244	1PW-5	1.72	0.96	512.31	741.51	11.61	6.16
0.305	1PW-6	1.75	0.96	356.60	399.89	0.73	7.7
0.366	1PW-7	1.76	1.02	250.13	478.95	9.11	9.24
0.427	1PW-8	1.75	0.99	240.03	453.36	8.38	10.8
0.488	1PW-9	1.76	0.99	285.84	449.76	7.00	12.3
0.549	1PW-10	1.75	0.93	277.65	429.49	4.07	13.9
0.61	1PW-11	1.76	0.96	248.38	454.64	9.02	15.4
							0

MPa	370.99	575.10	9.35
±	113.99	152.22	4.80
ksi	53.81	83.41	
±	16.53	22.08	

0	1PW-1	1.67	0.77	438.31	567.60	3.15	0
0.061	1PW-2	1.67	0.99	412.45	679.12	15.10	1.54
0.122	1PW-3	1.67	0.91	417.00	626.51	4.33	3.08
0.183	1PW-4	1.68	0.95	322.14	524.91	2.56	4.62
0.244	1PW-5	1.67	0.91	308.64	529.82	4.41	6.16
0.305	1PW-6	1.72	0.96	245.06	418.10	5.57	7.7
0.366	1PW-7	1.70	0.99	244.12	462.04	9.66	9.24
0.427	1PW-8	1.70	0.96	253.43	454.69	9.14	10.8
0.488	1PW-9	1.70	0.97	244.84	451.75	9.34	12.3
0.549	1PW-10	1.70	0.96	245.86	451.33	8.09	13.9
0.61	1PW-11	1.73	0.96	232.52	433.70	8.45	15.4

1PASS FSP OVER FW BLOCK +2

MPa	305.85	509.05	7.25
±	80.30	85.18	3.68
ksi	44.36	73.83	
±	11.65	12.35	

0	1PW-1	1.67	0.99	443.74	529.09	1.43	0
0.061	1PW-2	1.70	0.97	410.00	495.00	1.20	1.54
0.122	1PW-3	1.72	1.00	382.13	459.97	0.92	3.08
0.183	1PW-4	1.68	0.99	276.24	439.71	2.07	4.62
0.244	1PW-5	1.68	0.99	268.04	477.99	5.57	6.16
0.305	1PW-6	1.73	1.01	233.96	448.26	9.56	7.7
0.366	1PW-7	1.71	1.01	242.73	430.03	7.86	9.24
0.427	1PW-8	1.72	1.01	235.50	447.90	9.08	10.8
0.488	1PW-9	1.73	1.02	233.62	455.89	12.23	12.3
0.549	1PW-10	1.73	1.01	224.34	435.38	10.10	13.9
0.61	1PW-11	1.72	1.01	218.52	445.64	9.53	15.4

1PASS FSP OVER FW BLOCK -1

MPa	288.07	460.44	6.32
±	82.52	29.57	4.22
ksi	41.78	66.78	
±	11.97	4.29	

THIS PAGE INTENTIONALLY LEFT BLANK

LIST OF REFERENCES

1. W.M Thomas et.al., “Friction Stir Butt Welding”, International Patent Appl.No. PCT/GB92/02203 and GB Patent Appl. No. 9125978.8, Dec 1991, U.S. Patent No. 5,460,317 – from [Ref. 2] in support of information by Stephan Dallee and David Nicholas, TWI.
2. Mishra, R.S. and Mahoney, M.W., “Friction Stir Processing: A New Grain Refinement Technique to Achieve High Strain Rate Superplasticity in Commercial Alloys,” *Materials Science Forum*, v. 357-359, p. 507-514, 2001.
3. Culpan, E.A. and Rose, G., “Microstructural Characterization of Cast Nickel Aluminum Bronze,” *Journal of Materials Science*, v.13,p. 1647-1657, 1978.
4. Culpan, E.A. and Rose, G., “Corrosion Behavior of Cast Nickel Aluminum Bronze in Sea Water,” *British Corrosion Journal*, v.14, p.160-166, 1979.
5. Weston, G.M., “Survey of Nickel-Aluminum Bronze Casting Alloys on Marine Applications,” Australia Dept. of Defence Report, DSTO MRL, Melbourne, Victoria, MRL-R-807, 1981
6. F.Hasan, A. Jahanafrooz, G.W. Lorimer and N. Ridley, “The Morphology, Crystallography, and Chemistry of Phases in As-Cast Nickel-Aluminum Bronze,” *Met. Trans A*, v.13a, p. 1337-1345, 1982.
7. F.Hasan, g.W. Lorimer and N.Ridley, “Crystallography of Martensite in a Cu-10Al-5Ni-5Fe alloy,” *Journal de Physique*, v.43, p.C4 653-C4 658, 1982.
8. R.S Mishra: *Advanced Material and Processes*, 2003, vol. 161(10), pp. 43-46 9. R.S Mishra, Z.Y. Ma and I. Charit: *Mater. Sci. Engng. A*, 2003, vol. A341, pp.307-310
10. Z.Y. Ma, R.S. Mishra and M.W. Mahoney: *Friction Stir Welding and Processing II*, K.V.Jata, M.W. Mahoney, R.s. Mishra, S.L. Semiatin and T. Lienert, eds., TMS, Warrendale, PA, 2003, pp. 221-30
11. Oh-Ishi, Keiichiro, McNelley, T.R; Microstructural Modification of As-Cast NiAl Bronze Friction Stir Processing, *Metallurgical and Materials Transactions*, vol.35A, September 2004
12. Kou, Sindo, Welding Metallurgy Second Edition, John Wiley & Sons, Inc.,© 2003, p.57
13. Kou, Sindo, Welding Metallurgy Second Edition, John Wiley & Sons, Inc.,© 2003, pp. 156-159

14. Magula, V., Liao, J., Ikeuchi, K., Kuroda, T., Kikuchi, Y., and Matsuda, F., *Trans. Japn. Weld Res. Inst.*, 25:49, 1996
15. Kou, Sindo, Welding Metallurgy Second Edition, John Wiley & Sons, Inc., © 2003, p.263
16. Sahoo, M., “Weldability of Nickel-Aluminum Bronze Alloy C95800,” *AFS Trans*, v. 112, p. 893-911, 1982.

INITIAL DISTRIBUTION LIST

1. Defense Technical Information Center
Ft. Belvoir, VA
2. Dudley Knox Library
Naval Postgraduate School
Monterey, CA
3. Dr. Terry R. McNelley
Department of Mechanical and Astronautical Engineering
Naval Post Graduate School, Monterey, CA
4. Dr. Anthony J. Healey
Chairman, Department of Mechanical and Astronautical Engineering
Naval Post Graduate School, Monterey, CA
5. Naval Surface Warfare Command (NSWC) Carderock
Bethesda, MD